Journal of Quantitative Spectroscopy & Radiative Transfer 329 (2024) 109211

Contents lists available at ScienceDirect

Journal of Quantitative Spectroscopy and Radiative Transfer

journal homepage: www.elsevier.com/locate/jqsrt

Demonstration of a physical inversion scheme for all-sky, day-night IASI observations and application to the analysis of the onset of the Antarctica ozone hole: Assessment of retrievals and consistency of forward modeling

Carmine Serio [a,*], Guido Masiello [a], Giuliano Liuzzi [a], Angela Cersosimo [a], Tiziano Maestri [b], Michele Martinazzo [b], Fabrizio Masin [b], Giorgia Proietti Pelliccia [b], Sara Venafra [c], Claude Camy-Peyret [d]

[a] Scuola di Ingegneria, Università della Basilicata, Potenza, Italy
[b] DIFA, Università di Bologna, Bologna, Italy
[c] Agenzia Spaziale Italiana, ASI, Roma, Italy
[d] Institut Pierre-Simon Laplace, IPSL, Paris, France

ARTICLE INFO

Keywords:
All sky radiative transfer
Retrieval in cloudy antarctic atmosphere
Satellite
Infrared
Ozone hole
Stratospheric ice clouds

ABSTRACT

Based on a recently developed all-sky forward model (σ-IASI/F2N) for the computation of spectral radiances in the range 100 to 2760 cm^{-1}, the paper addresses the spring onset of the Antarctica ozone hole with infrared observations from the IASI (Infrared Atmospheric Sounder Interferometer) satellite sounder. The Antarctica ozone hole is a cyclic event that grows in normal conditions in late August and collapses in late November/early December. Because of climate change (cooling of the stratosphere), the O_3 hole is expected to become deeper. Indeed, 2021 and 2023 have been characterized by very spatially extensive and deep ozone hole. To demonstrate that we can gain further insights into these phenomena with the help of infrared nadir viewing observations, we have developed an all-sky retrieval tool, which inverts the whole IASI infrared spectrum to simultaneously estimate thermodynamic and geophysical parameters, including ozone and nitric acid, which are key parameters in analyzing the Antarctic ozone hole. Infrared sounders acquire data day and night, unlike visible and ultraviolet sounders, which are only operational during daytime. This enables us to acquire data also during the polar night, which is a critical time for O_3 hole formation. Ice polar stratospheric clouds have been identified and fitted with our scheme. Maps of atmospheric ozone, complemented with those of nitric acid, temperature, and lower stratosphere height, have been retrieved for July, September, and October 2021 and 2023. Results are compared to those derived from TROPOMI (TROPOspheric Monitoring Instrument) and OMI (Ozone Monitoring Instrument), showing a very good agreement. The comparison of simultaneously retrieved O_3 and HNO_3 shows that the onset of the ozone hole is associated with relevant denitrification in the Antarctica Stratosphere. For 2023, our findings also show that O_3 depletion episodes began as early as July. Although demonstrative, our analysis evidences the importance of Numerical Weather Prediction centers to assimilating all-sky infrared radiances (day, night, clear, or with ice or water clouds) to get insights into providing a more comprehensive picture of the Southern Spring ozone depletion over Antarctica.

1. Introduction

According to the Copernicus Atmosphere Monitoring Service (CAMS, see e.g., https://atmosphere.copernicus.eu/twists-and-turns-2023-Southern-hemisphere-ozone-hole) the last three years (2021–2023) saw large, longer lasting than average Southern Hemisphere ozone hole seasons. The Antarctica ozone hole is governed by the photochemical destruction of the ozone molecule through a chemical reaction with chlorine, e.g., see Krummel et al. [1]. Various mechanisms have been proposed to explain ozone depletion. Polar stratospheric clouds (PSCs) formation is the fundamental catalytic mechanism that accelerates ozone destruction [2]. Polar stratospheric clouds formation involves HNO_3 and H_2O initially in the gas phase, which then condense into the solid phase (giving rise to crystals of HNO_3–$3H_2O$ or NAT) at

* Corresponding author.
E-mail address: carmine.serio@unibas.it (C. Serio).

https://doi.org/10.1016/j.jqsrt.2024.109211
Received 5 April 2024; Received in revised form 24 September 2024; Accepted 30 September 2024
Available online 5 October 2024

temperatures below 195 K as shown in the review paper [2] and discussed in the section on PSCs below. The mechanism and chemistry of the formation of PSCs and the destruction of O_3 have been assessed using satellite observations. Noteworthy is the analysis performed with the Michelson Interferometer for Passive Atmospheric Sounding (MIPAS) [3–5], the Cloud-Aerosol Lidar with Orthogonal Polarization (CALIOP) [6–10] and the Microwave Limb Sounder (MLS) [11]. Until now, this phenomenon has been investigated and continuously monitored with a suite of satellite instruments, among which the Ozone Monitoring Instrument, OMI (https://aura.gsfc.nasa.gov/omi.html), and the TROPOspheric Monitoring Instrument, TROPOMI (https://www.tropomi.eu/). While sensitive to ozone, aerosols, and some other specific species like BrO, none of the mentioned above instruments is neither sensitive to the thermodynamic conditions of the polar altitudes extending from the Upper Troposphere to the Lower Stratosphere (UT/LS region), nor capable of sensing nitric acid and water in the gas phase. We also mention that the UT/LS region can be sensed with microwave instruments (e.g., MLS), [12]); however, they have low horizontal spatial resolution compared to infrared instruments.

This work focuses on nadir-view, high spectral resolution infrared observations. The objective of the study is to demonstrate that high spectral resolution infrared sounders can contribute to the continuous monitoring of the Antarctic ozone hole and provide information on other gas and thermodynamic parameters relevant to achieve better understanding of the ozone hole formation and climatology. To this end, we show the first analysis of the onset of the ozone hole with all-sky infrared observations recorded on Sept. 9, 2021 and 2023 from the IASI instrument [13] flying on the Meteorological Operational Satellites operated by EUMETSAT(European Organization for the Exploitation of Meteorological Satellites). In addition to the methodological aspects of retrieving atmospheric parameters in all-sky conditions, it is important to stress that the time evolution and analysis of O_3 and HNO_3 have already been the subject of many studies with IASI observations. Among many others, the studies presented in [14–17] are particularly relevant to the present work. What is novel in this work is the application of an all-sky forward model, which increases the amount of IASI soundings we can use and, hence, the spatial and temporal resolution.

This work has been possible thanks to recent improvements [18–20] of scaling approaches in radiative transfer in cloudy atmospheres, first introduced by [21]. The pseudo-monochromatic forward model used in this paper works with look-up tables to quickly calculate the optical depth of gas species and clouds. The model also considers multiple scattering effects by adopting suitable scaling of the radiative properties of clouds, following the same formalism used in clear sky conditions [20].

The retrieval tool has been used to estimate the vertical profiles of temperature, H_2O, HDO, O_3, ice, and liquid water contents simultaneously with other atmospheric gas constituents, including HNO_3. We stress that our algorithm is demonstrative and intended for science issues. Also, it should not be confused with the official IASI Level 2 product system released by EUMETSAT (see, e.g., https://data.eumetsat.int/extended?query=IASI). Furthermore, the official IASI level 2 product is a combined Microwave (ATOVS (Advanced TIROS -Television Infrared Observation Satellites- Operational Sounder) and MHS (Microwave Humidity Sounder) sensors)+Infrared (IASI) observations, and an official IASI stand-alone level 2 product does not exist. The retrieval system uses the IASI Level 1c spectral radiance and the ATOVS observations, namely AMSU-A (Advanced Microwave Sounding Unit) Level 1b, AVHRR (Advanced Very High Resolution Radiometer) Level 1b, MHS Level 1b. The IASI Level 2 processing also uses Numerical Weather Prediction (NWP) data. The system also has an Optimal Estimation module [22], applied only to clear sky soundings to retrieve temperature, water vapor, and ozone profiles.

The retrieval module builds upon the all-sky methodology presented in e.g., [23,24]. It implements an Optimal Estimation scheme and handles the dimensionality reduction of spectral data and parameter space through suitable transforms.

Other forward/inverse all-sky models exist that have been applied, e.g., to the Atmospheric Infrared Sounder (AIRS). Still, only very few use the entire spectral range of infrared observations. In this respect, the SARTA all-sky forward model developed by DeSouza-Machado et al. [25] is noteworthy. The main difference with our model is that we use the full cloud vertical profiles without reducing them to one or two slabs. We also mention the all-weather retrieval system developed by [26,27]; again, the difference with our system is that they represent the cloud with a single homogeneous layer. A retrieval system based on the multi-layer representation of clouds was developed by [28,29]. However, the state vector is less complex than in this work and omits, e.g., HDO. For completeness, we also cite the work by [30], where the retrieval is limited to bulk cloud parameters (cloud optical depth, top temperature, effective particle radius). Concerning Numerical Weather Prediction, the direct assimilation of all-sky IR radiances is not yet used operationally [31]. Finally, we also stress that our system works on a single Field Of View (FOV), and differs from many current infrared algorithms used for profile retrievals over a larger Field Of Regard (FOR) composed, e.g., by 3×3 or 2×2 FOVs for the purpose of cloud clearing or hole hunting, e.g., see [32]. The latter algorithms can definitely lower the horizontal spatial resolution of satellite infrared soundings.

The paper is organized into three sections. Section 2 details the data used in the study and presents the methodology's essential aspects, both forward and inverse modules. Section 3 describes the results, whereas Section 4 deals with conclusions and outlook.

2. Data and methods

IASI spectra and the analysis of the meteorological fields of ECMWF (European Centre for Mid-range Weather Forecasts) are used to define a co-registered data set of pairs (observations, atmospheric state vector) covering the Antarctica region (-60° to -90° in latitude) on July, August, September, and October 2021 and 2023. To demonstrate the potential of data+methods, we have focused our analysis on a single day (the 9th) of IASI soundings each month. We have chosen day 9 as the day representative of the month. September has been selected because the Austral spring begins that month, and the South Pole begins to get out of the polar night. July and August are taken for comparison because the South Pole is still in the polar night in those months, and, finally, in October, the southern polar region is in daylight. ECMWF analyses consist of atmospheric profiles of the state of the atmosphere at the synoptic hours 00:00, 06:00, 12:00, and 18:00 UTC, and they are used to define the first guess state vector for the inverse module. IASI spectra are paired with the ECMWF analyses, allowing a time window of ±15 min.

The spectral interval covered by the IASI detectors is 645- 2760 cm^{-1}, at a sampling of $\Delta\sigma$=0.25 cm^{-1}, giving a total of 8461 points per spectrum. The instrument has a swath width of ±1100 km, and the Instantaneous Field Of View (IFOV) is 12 km at nadir, whereas the FOR consists of 2×2 IFOVs. IASI takes millions of spectra daily over all latitudes, with most mid-latitude and tropical spots covered once in the daytime and once at night. These are not limited by Solar Zenith Angle or latitude, therefore polar regions are fully covered.

We use level 1C radiances, which are spectrally calibrated, geolocated, and Gaussian apodized (e.g., see [33]). The cloud mask is provided within the IASI native L1C data and computed using AVHRR (Advanced Very High-Resolution Radiometer) images recorded synchronized with IASI spectra. From the AVHRR cloud mask analysis, we also use the fractional cloud cover or cloud fraction, *cf*, in each IASI IFOV. The cloud mask is also used to detect clear sky, which corresponds to $cf \leq 5\%$; below such a threshold we consider $cf = 0$.

The ECMWF atmospheric state vector consists of surface temperature, T_s, profiles of air temperature, T, water vapor mixing ratio, Q, ozone mixing ratio, O, specific liquid, and ice water content (q_{LWC} and q_{IWC} expressed in mass mixing ratio, kg kg^{-1}) over a pressure grid of 137 levels, which covers the pressure range from the pressure surface to 0.01

hPa.

We have also collected the total O_3 column from OMI and TROPOMI for the same area and dates. OMI data are level 3 products and are provided on a grid of 0.25° × 0.25° ([34]| NASA's Earth Observing System, https://eospso.nasa.gov/sites/default/files/atbd/ATBD-OMI-02.pdf.), whereas TROPOMI ozone is level 2 data supplied at the native instrument spatial resolution 7 km × 3.5 km and processed according to [35].

2.1. The forward model

The forward model used in the present analysis has a strong heritage from the σ-IASI radiative transfer method [36]. It is a pseudo-monochromatic, fast code and computes the surface/atmosphere spectrum in the infrared and related Jacobian matrices. It takes advantage of improvements (e.g., [19]) for applying scaling methods (e.g., [21]) that parametrize the optical depth of ice and liquid water clouds and several aerosol species. The new version of the code is referred to as σ-IASI/F2N. Recent results [20] show that σ-IASI/F2N can use ECMWF meteorological analysis as input and reproduces cloud fields accurately.

The all-sky radiance is computed according to the additive model:

$$R(\sigma) = (1 - cf)R_{clear-sky} + cfR_{cloudy-sky} \quad (1)$$

With, again, *cf* the cloud fraction, $cf = 0$ means a clear FOV, and $cf = 1$ is a fully overcast FOV. Eq. (1) implements the maximum overlap model and says that the cloudy spectra are calculated as the linear combination of clear and cloudy columns based on the cloud fraction. $R(\sigma)$ is the spectrum calculated with the maximum overlap assumption, and *cf* is defined as the maximum cloud fraction in the cloud coverage profile. $R_{clear-sky}$ and $R_{cloudy-sky}$ are the clear-sky and the full overcast spectrum, respectively. In the case of the full overcast spectrum, we assume clouds fill the entire satellite footprint. Indeed, the forward model treats clouds as homogeneously distributed plane parallel layers. The cloud fraction *cf* is taken from the native IASI L1C cloud mask, which is based on the AVHRR imager. In the present work, we only analyze clear sky ($cf = 0$) and full overcast ($cf = 1$)IASI footprints.

Typical statistics for the number of IASI IFOVs covered by clouds show that only 2.5 % of IASI FOR (2 × 2 IFOVs) are completely clear sky. In contrast, 39 % of FOR are overcast ($cf = 1$) [32]. The overcast FOR cannot be dealt with in a cloud-clearing scheme [32] and, therefore, cannot be cloud-cleared and used in clear-sky-like retrieval systems. As a result, using an all-sky algorithm dramatically improves the density of IASI soundings available for retrieval purposes. Although outside the main objective of this study, an example of these improvements is shown in the supplemental material (see Fig. S1).

The σ-IASI/F2N model uses an appropriate atmospheric layering to compute optical depths. The layering consists of a fixed 60-layer pressure grid spanning the 1100–0.005 hPa range. The 61 atmospheric pressure levels, which divide the atmosphere into 60 layers, are shown in Fig. 1. The relatively higher density of layers at pressure levels just above the tropopause was specially conceived to optimize the retrieval of stratospheric gases such as ozone and nitric acid. The monochromatic optical depth calculation is based on suitable look-up tables for atmospheric species and clouds. For atmospheric species, the look-up table is generated from LBLRTM v.12.7 [37], and related MT_CKD v. 2.7 for water vapor continuum absorption. For clouds, we rely on the Ping Yang database [38,39] from which bulk optical properties are derived, as described in Maestri et al. [40] and [20]. For further details about the latest version of σ-IASI/F2N, we refer the readers to [20].

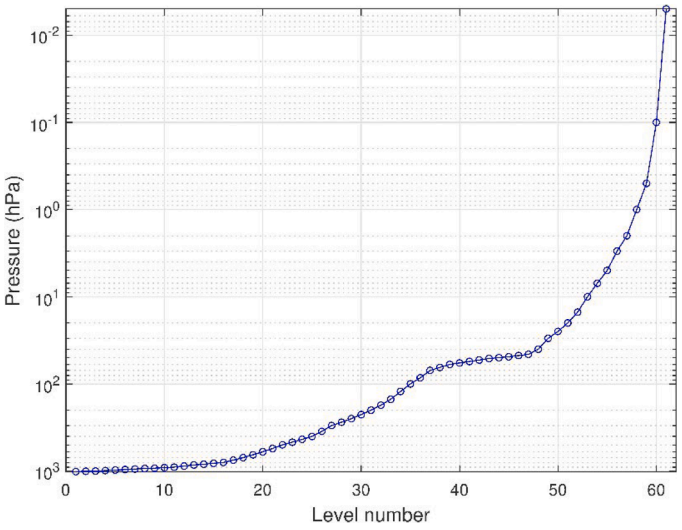

Fig. 1. The definition of the atmospheric pressure levels used in σ-IASI/F2N.

2.2. The inverse module

The inverse module follows the basic methodology described in [36], and its most recent implementation is described by [23,24]. In the present study, the inverse module estimates the following atmospheric state vector

$$\boldsymbol{\nu} = \left(\in, \boldsymbol{T}, T_s, \boldsymbol{Q}, \boldsymbol{O}, \boldsymbol{HDO}, \boldsymbol{q}_{LWC}, \boldsymbol{r}_e, \boldsymbol{q}_{IWC}, \boldsymbol{D}_e, \boldsymbol{q}_{CO_2}, \boldsymbol{q}_{N_2O}, \boldsymbol{q}_{CO}, \boldsymbol{q}_{CH_4}, \boldsymbol{q}_{SO_2}, \boldsymbol{q}_{HNO_3}, \boldsymbol{q}_{NH_3}, \boldsymbol{q}_{OCS}, \boldsymbol{q}_{CF_4}, w \right) \quad (2)$$

where T_s is the surface temperature, $\in$ is the spectral emissivity (8461 elements, the same number as the spectral radiances), $\boldsymbol{T}$ represents the air temperature profiles, $\boldsymbol{Q}$, $\boldsymbol{O}$, $\boldsymbol{HDO}$ are the mixing ratio profiles of water vapour, ozone and HDO. Furthermore, $\boldsymbol{q}_X$ represents the mixing ratio profiles of the given species *X*, listed in Eq. (2). The former profiles form the basis of the state vector for a clear sky. In the case of a cloudy sky, additional profiles are added for the mixing ratio of liquid and ice water, $\boldsymbol{q}_w$ and $\boldsymbol{q}_i$, respectively, and the profiles of related effective radii, $\boldsymbol{r}_e$ for *liquid water* clouds and dimension, $\boldsymbol{D}_e$ for ice clouds. There is one more scalar quantity, *w*, the average wind speed over oceans, which is only used in the clear sky during the daytime because it is an input parameter of the Cox-Munk BRDF model for sunglint modelling (over the cloud-free ocean). In clear sky and for land surface, we also retrieve the emissivity spectrum, which is represented with a PCA expansion, truncated at the first $\tau = 20$ PC scores (e.g., [41]).

The position of a given parameter (scalar or sub-vector) in the full-state vector is just a matter of choice. It does not reflect any physical constraint or relationship among the various components. More specifically, the background matrix of the state vector is block-diagonal, in which each diagonal block is dedicated to a given parameter, e.g., $\boldsymbol{T}$, $\boldsymbol{Q}$ or $\boldsymbol{q}_{CO_2}$. In its cloudy sky version, the state vector contains 1020 elements, corresponding to as many degrees of freedom. This number of elements is too large to be handled in the retrieval algorithm. We set up various strategies to reduce the dimensionality of observation data and parameter space.

For the parameter space, the seven vectors $\boldsymbol{q}_{CO_2}$, $\boldsymbol{q}_{N_2O}$, $\boldsymbol{q}_{CO}$, $\boldsymbol{q}_{SO_2}$, $\boldsymbol{q}_{NH_3}$, $\boldsymbol{q}_{OCS}$, $\boldsymbol{q}_{CF_4}$ are dealt with a scalar scaling factor so that the inverse tool estimates the column amount. For the given species X, we assume $\boldsymbol{q}_X$

$= (1 + f_X)\boldsymbol{q}_{a,X}$ where $\boldsymbol{q}_{a,X}$ is a suitable background profile. Depending on the application, the scheme can retrieve the profile of one or more trace gases. For the present study, this is, e.g., the choice for HNO_3 (see Section 2.2.1).

Liquid water and ice mixing ratio profiles, $\boldsymbol{q}_{LWC}$, $\boldsymbol{q}_{IWC}$ are transformed from the physical space to a truncated PCA series of 10 scores each. To this end, we use the global ECMWF Reanalysis version 5 (ERA5, see, e.g., https://confluence.ecmwf.int/display/CKB/ERA5) to build up the orthogonal PCA basis. The effective liquid water radius and the effective size of ice particles have been derived from the Wyser model for ice [42] and the Martin model for liquid water [43].

With this in mind, the state vector we retrieve with the inverse algorithm is

$$\boldsymbol{v} = \left(\boldsymbol{c}_{\in}, \boldsymbol{T}, T_s, \boldsymbol{Q}, \boldsymbol{O}, \boldsymbol{HDO}, \boldsymbol{q}_{HNO_3}, \boldsymbol{c}_{LWC}, \boldsymbol{c}_{r_e}, \boldsymbol{c}_{IWC}, \boldsymbol{c}_{D_e}, f_{CO_2}, f_{N_2O}, f_{CO}, f_{CH_4}, f_{SO_2}, f_{NH_3}, f_{OCS}, f_{CF_4}, w\right) \tag{3}$$

where $\boldsymbol{c}_X$ is a vector of PC scores for the given cloud parameter X, and f_X is the scaling factor for the given gas species X. Note that the vector of 20 PC scores for emissivity, $\boldsymbol{c}_{\in}$, is included in the state vector only for land surface and clear sky. The scalar wind parameter w is included only for sea surface and clear sky. Finally, note that for HNO_3 we retrieve the whole profile given its role in contributing to the formation of PSCs (e.g., [2]).

With the simplification introduced in the state vector, we must retrieve at most $N = 350$ scalar parameters. These parameters are simultaneously retrieved through the Optimal Estimation methodology [22].

The estimator, $\hat{\boldsymbol{v}}$ of the state vector, $\boldsymbol{v}$ is given by

$$\hat{\boldsymbol{v}} = \boldsymbol{v}_a + \left(\boldsymbol{K}^t\boldsymbol{S}_\varepsilon^{-1}\boldsymbol{K} + \boldsymbol{S}_a^{-1}\right)^{-1}\boldsymbol{K}^t\boldsymbol{S}_\varepsilon^{-1}(\boldsymbol{y} - \boldsymbol{K}\boldsymbol{v}_a) = \boldsymbol{v}_a + \left(\boldsymbol{K}^t\boldsymbol{S}_\varepsilon^{-1}\boldsymbol{K} + \boldsymbol{S}_a^{-1}\right)^{-1}\boldsymbol{K}^t\boldsymbol{S}_\varepsilon^{-1}\boldsymbol{K}(\boldsymbol{v} - \boldsymbol{v}_a) \tag{4}$$

with: $\boldsymbol{v}_a$,$\boldsymbol{S}_a$, the background state vector and covariance, respectively; $\boldsymbol{K}$ the usual derivative matrix or Jacobian; $\boldsymbol{y}$, $\boldsymbol{S}_\varepsilon$ the observations (vector of size M) and related covariance matrix. We make here the linear approximation $\boldsymbol{y} = \boldsymbol{K}\boldsymbol{v}$, with $\boldsymbol{v}$ the true state vector (size N). Considering that the matrix, $\boldsymbol{S}_\varepsilon$ is symmetric, we also have $\boldsymbol{K}^t\boldsymbol{S}_\varepsilon^{-1}\boldsymbol{K} = \boldsymbol{K}^t\boldsymbol{S}_\varepsilon^{-t/2}\boldsymbol{S}_\varepsilon^{-1/2}\boldsymbol{K} = \left(\boldsymbol{S}_\varepsilon^{-\frac{1}{2}}\boldsymbol{K}\right)^t\left(\boldsymbol{S}_\varepsilon^{-\frac{1}{2}}\boldsymbol{K}\right) = \boldsymbol{J}^t\boldsymbol{J}$, with $\boldsymbol{J} = \boldsymbol{S}_\varepsilon^{-\frac{1}{2}}\boldsymbol{K}$, the normalized Jacobian matrix. Therefore, Eq. (4) becomes

$$\hat{\boldsymbol{v}} = \boldsymbol{v}_a + \left(\boldsymbol{J}^t\boldsymbol{J} + \boldsymbol{S}_a^{-1}\right)^{-1}\boldsymbol{J}^t\boldsymbol{J}(\boldsymbol{v} - \boldsymbol{v}_a) \tag{5}$$

The AK matrix [22] allows for calculating degrees of freedom (*dof*); it is computed according to:

$$\boldsymbol{A} = \frac{\partial\hat{\boldsymbol{v}}}{\partial\boldsymbol{v}} = \left(\boldsymbol{J}^t\boldsymbol{J} + \boldsymbol{S}_a^{-1}\right)^{-1}\boldsymbol{J}^t\boldsymbol{J} \tag{6}$$

In our inverse problem, where $\hat{\boldsymbol{v}}$ is made up of unlike quantities (e.g., temperature, water vapor, and so on) and where the size of $\boldsymbol{J}$ is $M(= 8461) \times n(\approx 350)$, Eqs. (5) and (6) are not suitable for numerical calculations because the kernel $\left(\boldsymbol{J}^t\boldsymbol{J} + \boldsymbol{S}_a^{-1}\right)$ is usually singular within working numerical precision. The singularity is largely coming from the presence of the inverse of $\boldsymbol{S}_a$. A procedure to eliminate such singularity is adopted here following the method developed by [44] and is fully explained in [24]. For the benefit of the reader, the procedure is outlined below.

If we normalize the state vector according to

$$\boldsymbol{x} = \boldsymbol{S}_a^{-\frac{1}{2}}\boldsymbol{v};\ \boldsymbol{x}_a = \boldsymbol{S}_a^{-\frac{1}{2}}\boldsymbol{v}_a;\ \hat{\mathbf{x}} = \boldsymbol{S}_a^{-\frac{1}{2}}\hat{\boldsymbol{v}} \tag{7}$$

and consider the twice-normalized Jacobian [45],

$$\mathbf{G} = \boldsymbol{S}_\varepsilon^{-\frac{1}{2}}\boldsymbol{K}\boldsymbol{S}_a^{\frac{1}{2}} \tag{8}$$

then Eq. (5) can be put in a form that is fully non-dimensional and non-singular (because $\boldsymbol{S}_a^{-1}$ is replaced with the Identity matrix $\boldsymbol{I}$).

The normalized, optimal estimation for $\hat{\mathbf{x}}$, can be written as

$$\hat{\mathbf{x}} = \boldsymbol{x}_a + \left(\boldsymbol{G}^t\boldsymbol{G} + \boldsymbol{I}\right)^{-1}\boldsymbol{G}^t\boldsymbol{G}(\boldsymbol{x} - \boldsymbol{x}_a) \tag{9}$$

Thus, the normalized averaging kernel

$$\tilde{\mathbf{A}} = \frac{\partial\hat{\mathbf{x}}}{\partial\boldsymbol{x}} = \left(\boldsymbol{G}^t\boldsymbol{G} + \boldsymbol{I}\right)^{-1}\boldsymbol{G}^t\boldsymbol{G} \tag{10}$$

which is fully dimensionless. Combining Eq. (9) with Eq. (8), we also obtain the linear relationship,

$$\hat{\boldsymbol{x}} = \boldsymbol{x}_a + \tilde{\mathbf{A}}(\boldsymbol{x} - \boldsymbol{x}_a) = \tilde{\mathbf{A}}\boldsymbol{x} + (\boldsymbol{I} - \tilde{\boldsymbol{A}})\,\boldsymbol{x}_a \tag{11}$$

in which the estimate $\hat{\boldsymbol{x}}$ relates to the background and true state vectors, $\boldsymbol{x}_a$, $\boldsymbol{x}$, respectively. Eq. (11) says that our estimate is identical to the true state provided that $\tilde{\boldsymbol{A}} = \boldsymbol{I}$, the identity matrix.

Finally, we quote that the estimated $\hat{\mathbf{x}}$ and the normalized $\tilde{\boldsymbol{A}}$ can be transformed back to the physical parameter space according to $\hat{\mathbf{v}} = \boldsymbol{S}_a^{\frac{1}{2}}\hat{\mathbf{x}}$; $\boldsymbol{A} = \boldsymbol{S}_a^{\frac{1}{2}}\tilde{\boldsymbol{A}}\,\boldsymbol{S}_a^{-\frac{1}{2}}$. Because of the *trace* theorem, we have $dof = trace\,(\boldsymbol{A}) = trace\,(\tilde{\boldsymbol{A}})$ that is, the *dof* remains invariant under the normalizing transform.

2.2.1. Background, first guess, and degree of freedom

Besides cloud parameters, the first guess, the background state vector, and its covariances are built up as described in [23]; they are summarized here for the reader's benefit. For a correct understanding of the many data sources we use and how we use them, we anticipate that a summary is provided in Table 2.

2.2.1.1. Emissivity. The emissivity is only retrieved over clear sky land surface, and the CAMEL (Combined ASTER MODIS Emissivity over Land) database [46] is used for the first guess. The interpolation from the 13 CAMEL hinge points to the IASI spectral resolution is performed with a PCA algorithm [47]. For the background vector and related covariance matrix, we use the emissivity database obtained by the ASTER (Advanced Spaceborne Thermal Emission Reflection Radiometer) Spectral Library version 2.0 [48] and the MODIS (Moderate Resolution Imaging Spectrometer) UCSB (University of California, Santa

Barbara) Emissivity Library (http://www.icess.ucsb.edu/modis/EMIS/html/em.html). The resulting ensemble of data is used to build up the PCA transform and basis to project the emissivity at IASI spectral resolution. In there, we retain 20 PC scores. The retrieval system retrieves the PC scores, and the covariance matrix is set to the identity matrix because the PCs are orthogonal. Further details can be found in [41].

The emissivity is not retrieved for cloudy and clear sea surfaces and is fixed to that of the Masuda model [49]. Also, for cloudy land, the emissivity is not retrieved, and is kept fixed at the CAMEL database values.

2.2.1.2. Surface temperature, temperature, water vapor, and ozone profiles. For the thermodynamical parameters, T_s, $\boldsymbol{T}$, $\boldsymbol{Q}$, and ozone, $\boldsymbol{O}$, the covariance matrix has been built on global ECMWF analyses. We consider one day per month (the 15th) in the reference year 2018. The ensemble is space-localized in five climatological zones: High-latitude North (latitude 90 to 60°); Mid-latitude North (60 to 35°); Tropical (35 to −35°); Mid-latitude South (−35 to −60°); High-latitude South (−60 to −90°). Also, we distinguish between land and sea. Examples of covariances matrices for the case at hand are shown in the supplemental material (Figs. S2 to S4).

The First Guess is the space-time collocated ECMWF analysis. The $\boldsymbol{T}$, $\boldsymbol{Q}$, and $\boldsymbol{O}$ profiles have no transformation or truncation. They remain in the physical space and are represented on the same layers as those used in the forward model. These data are directly accessed through the ECMWF *ecgate service* (https://www.ecmwf.int/en/computing/access-computing-facilities), which should not be confused with the Copernicus data service.

2.2.1.3. HDO. Background and First Guess for HDO are derived from water vapor by proper multiplication by the abundance ratio D/Q prescribed in the Standard Reference Material Vienna Mean Ocean Water (VSMOW), RVSMOW=3.1×10^{-4}.

2.2.1.4. CO_2. As already mentioned, for CO_2 the profile is represented according to

$$\boldsymbol{q}_{CO_2} = \left(1 + f_{CO_2}\right)\boldsymbol{q}_{a,CO_2} \tag{12}$$

where $\boldsymbol{q}_{a,CO_2}$ is a suitable background profile. The retrieval system estimates f_{CO_2}; the background and First Guess values are set to zero, and the standard deviation of the background is 0.05. This value has been chosen by trial and error and takes into account the low time-space variability expected for CO_2.

The background profile is time and space-dependent and, when available, is set to the collocated profiles derived from the CAMS (Copernicus Atmospheric Monitoring Service) global greenhouse gas reanalysis (EGG4, https://ads.atmosphere.copernicus.eu/cdsapp#!/dataset/cams-global-atmospheric-composition-forecasts?tab=overview). At the date of this study, the reanalysis was available up to December 2020. Alternatively, we have used the profiles provided by the model developed by [50]. The model captures the salient features of the CO_2 profile, including the decrease in the stratosphere because of the mean age of stratospheric air [51]. An example of the CO_2 profile for latitudes and dates related to the present analysis is shown in the supplemental material (Fig. S5).

The retrieval of CO_2 is the most critical part of the inverse system because CO_2 channels are also used for temperature. CO_2 is retrieved using the hot or laser bands between 800 and 1200 cm^{-1}, which are mainly sensitive to the lower atmosphere. This spectral segment is not used to retrieve temperature, and its Jacobian is forced to zero. Conversely, the temperature profile is retrieved using the remaining channels, 645 to 800 cm^{-1}, and 1200 to 2760 cm^{-1}, and the Jacobian of CO_2 is set to zero for the latter channels. The procedure is detailed in [24]. Our retrieval scheme can also retrieve the CO_2 profile, which is not done in the present study, to save space in the state vector for the HNO_3 profile (see Section 2.2.1.9)

Table 1
Summary of the background and standard deviation of all the gas scaling factors used in the present version of the inverse model.

Gas	Background and first guess of the scaling factors	The standard deviation of the scaling factors
CO_2	0	0.05
CH_4	0	0.1
CO	0	0.2
N_2O	0	0.1
SO_2	0	100
NH_3	0	10
OCS	0	0.5
CF_4	0	2

2.2.1.5. CH_4 and CO. Methane and carbon monoxide are dealt with similarly to CO_2 (see Eq. (12)). Again, the background and First Guess scaling factors are set to zero, and the standard deviations are 0.1 for methane and 0.2 for carbon monoxide. For both gases, the background profile is derived from the CAMS global atmospheric composition forecasts (https://ads.atmosphere.copernicus.eu/cdsapp#!/dataset/cams-global-atmospheric-composition-forecasts?tab=overview). The forecast considered is that generated at 12:00 UTC. For CO, the standard deviation is set to 0.2 because its variability is larger than the long-lived species CH_4. As for CO_2, the retrieval system can alternatively retrieve the CH_4 profile, which is not done to allow for the complete HNO_3 profile in the state vector.

2.2.1.6. N_2O, SO_2, NH_3, OCS, CF_4. Again, these gases are represented in the same way as CO_2. The background and First Guess profiles are derived from climatology [52], and the background and First Guess scaling factors are set to zero. The background is static for this group of gases, not changing with time and space. Still, we allow for relatively larger standard deviations, which account for a more significant variability, especially of non-long-lived species. The background and standard deviation of all the scaling factors, including CO_2, CO, and CH_4, is summarized in Table 1.

2.2.1.7. The wind speed parameter, w. The wind speed parameter is used only for sea surface in clear sky. Its background and First Guess is 5 m s^{-1} with a standard deviation of 1 m s^{-1}.

2.2.1.8. Cloud parameters. For cloud parameters, we use the ECMWF ERA5 reanalysis (https://confluence.ecmwf.int/display/CKB/ERA5), which should not be confused with the ECMWF *ecgate service*. The ERA5 products are used to build up the background of cloud parameters, but not the First Guess.

We use the hourly data at the four synoptic hours, 00:00, 00:06, 12:00, 18:00 UTC, for the vector.

$$\boldsymbol{v}_{ECMWF} = (\boldsymbol{T}, T_s, \boldsymbol{Q}, \boldsymbol{O}, \boldsymbol{q}_{LWC}, \boldsymbol{q}_{IWC}) \tag{13}$$

Using the Wyser [42] and Martin [43] models, we then compute $\boldsymbol{r}_e$, $\boldsymbol{D}_e$. The set of $\boldsymbol{q}_{LWC}$, $\boldsymbol{q}_{IWC}$, $\boldsymbol{r}_e$, $\boldsymbol{D}_e$ is then used to build the PCA basis and background state and covariances. The ERA5 data used in the present analysis refers to the global analyses on the day 15th of each month for the year 2020.

The $\boldsymbol{q}_{LWC}$, $\boldsymbol{q}_{IWC}$, $\boldsymbol{r}_e$, $\boldsymbol{D}_e$ profiles are represented with 10 PC scores, which ensure the integrated quantity, such as liquid and ice water paths, are preserved. In general, 10 PC scores also represent the profiles well. An example is shown in the supplemental material (see Fig. S6). The covariance matrix of the background is the identity matrix because of the orthogonality of PC scores.

The ECMWF model analysis (accessed through the ECMWF *ecgate*

Table 2
Summary of the data store we use to build the background and fix the First Guess state parameters.

Parameter	Data Archive		Note
	Background vector and covariance	First Guess/ reference profile	
Ts, T, Q, O	ECMWF ecgate service*	ECMWF ecgate service*	
q_{LWC},q_{IWC}	ERA5	ECMWF ecgate service*	
CO_2		EGG4	If data are not available, we use the model by [50]
CO, CH_4		CAMS global atmospheric composition forecasts	
N_2O, SO_2, NH_3, OCS, CF_4		[52]	
Emissivity land, clear sky	ASTER Spectral Library version 2.0; MODIS UCSB Emissivity Library	Camel database [46]	Emissivity is not retrieved and set to the Camel database's prescribed values for cloudy conditions.
Emissivity, sea surface			Emissivity is not retrieved and set according to the Masuda model [49].

* Need a privileged access.

service), co-registered with the actual IASI soundings, is used as a first guess (FG) to initialize the inverse algorithm. We stress that the ECMWF analyses are used as First Guess in clear and cloudy conditions. In cloudy conditions, because of the short time scale variability of clouds, $\boldsymbol{q}_{LWC}$, $\boldsymbol{q}_{IWC}$ could be quite incorrect (e.g., [53]). For this reason, we use only ECMWF profiles, which are colocated with IASI observation within a time slot of ±15 min. Finally, we note that the ECMWF *ecgate service* has no date restriction for the availability of profiles, which can be accessed in real-time. This is why we use this privileged access for the First Guess profiles. For the benefit of the reader, Table 2 summarizes the many data services we use in our retrieval scheme. The driver to use one rather than another is just data availability.

We caution that the choice of using 10 PC scores to represent clouds' profile comes from an in-depth assessment of retrieval performances [20,54]. In the retrieval, the effective number of *dof* for cloud parameters depends indeed on the cloud type. For example, cases such those with optically thick liquid water clouds will rely mostly on background information, differently from optically thin ice clouds, characterized by bright spectral features.

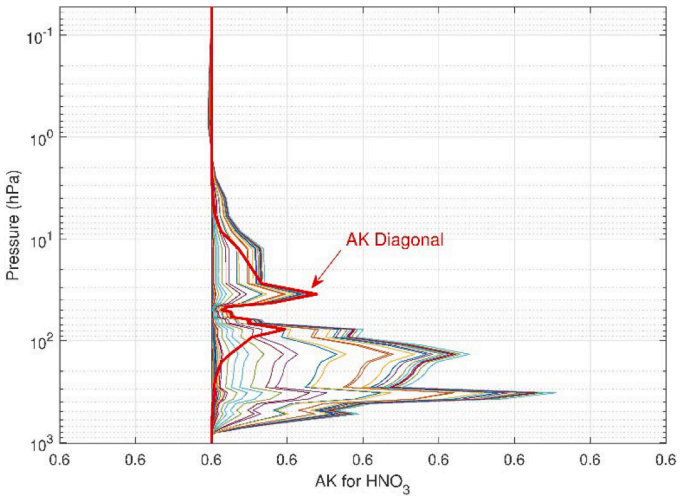

Fig. 3. Averaging Kernels for HNO_3 and its diagonal. The curves in the Figure have been obtained by averaging some 4000 IASI soundings. The sum of the diagonal terms is 0.9978.

2.2.1.9. HNO_3. HNO_3 is retrieved on the same layers as those used for forward modeling in a way that wants to be maximally committed to the IASI data. According to previous works (e.g. [55,56,57]), we consider a Markov-type matrix to model the background covariances of the HNO_3 profile,

$$S_a(i,j) = s(i)\,s(j)\,exp\left(-\frac{|p_i - p_j|}{\alpha p_o}\right) \tag{14}$$

with p_i the layer mean pressure i ($i = 1, \ldots, N_L$)and p_o, α are free parameters that allow us to tune the covariances and the inter-level correlation. Finally, s is a suitable standard deviation, which may be a function of pressure. For the present analysis, we set $p_o = 1000$ hPa, α = 0.01, and s is scaled with the layer pressure as shown in [58], to whom the reader is referred for further details. The background profile used for HNO_3 is static (that is, it does not change with time and space) and is shown in Fig. 2 with the background standard deviation s. The large values for s tend to mitigate the dependence of the final retrieval product concerning the chosen background. In other words, we seek a solution closer to the unconstrained least squares region, which depends on the

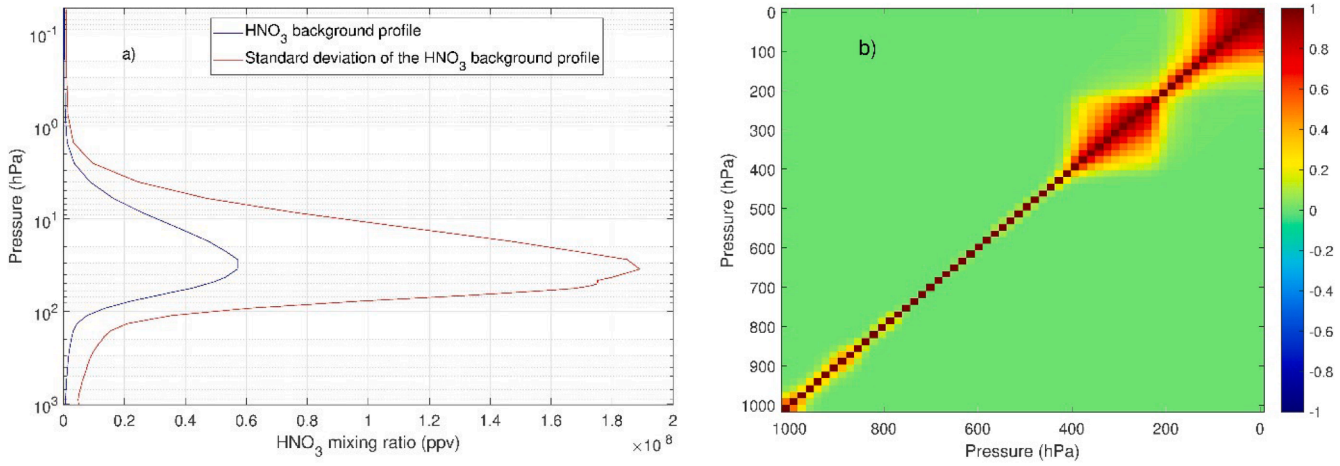

Fig. 2. (a) background profile for HNO_3 and its variability (standard deviation) assumed for the present analysis. (b) panel: full correlation matrix computed based on Eq. (13) and parameters shown in the left panel.

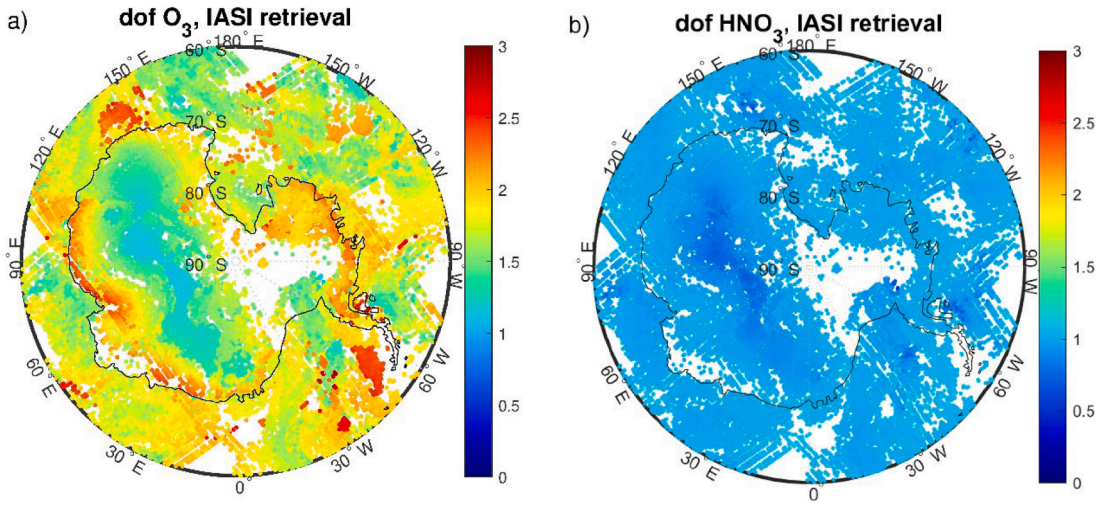

Fig. 4. *dof* for ozone (panel a) and nitic acid (panel b) corresponding to the IASI soundings on Sept. 9, 2021, for which we had converged retrievals.

data alone. The full covariance matrix computed according to Eq. (14) is shown again in Fig. 2 (right panel). It has been normalized so that it corresponds to the correlation matrix.

2.2.1.10. Degrees of freedom for O_3 and HNO_3. The present analysis is mainly devoted to the all-sky retrievals of ozone and HNO_3 profiles over the Antarctic region. Based on the background profiles and relative covariance matrix shown in Section 2.2.1.9, we have found that IASI observations have sensitivity to HNO_3 in the lower and middle stratosphere, as seen in Fig. 3, where we show typical stratospheric averaging kernels for HNO_3 in the case of a cloudy sky.

We see that there are large peaks in the tropospheric layers. However, they come from off-diagonal terms, add correlation along the profile, and do not add any *dof*. Fig. 4 also shows the plot of the diagonal of the Avergaing Kernels matrix, whose summation yields the total degree of freedom. A significant contribution to *dof* comes from 0 to 100 hPa range layers. The example shown in Fig. 4 suggests that IASI data are sensitive to the actual concentration of HNO_3 in the UT/LS region, where it is likely that we find the bulk of the stratospheric HNO_3 concentration (see e.g., Fig. 2) since there is no primary pollution source from the surface in Antarctica, which means that the tropospheric off-diagonal peaks occur in the atmospheric region where the HNO_3 profile is nearly zero.

Usually, the *dof* for ozone is ~2 or more, depending on location and air mass type. For the Antarctica region, a map of *dof* corresponding to the all-sky IASI soundings for Sept. 9, 2021, for which we had valid retrievals, is shown in Fig. 4. It is seen that the *dof* never goes below 1 (the average value over the area of interest is 1.68), meaning that the signal for ozone is large enough to retrieve ozone information from the IASI spectra data.

Again, from Fig. 4, it is seen that for HNO_3 the *dof* is $\cong$ 1 (the average over the area of interest is 0.96), indicating that the IASI information content for HNO_3 is large enough to retrieve information from the spectra for the total column amount of this species. Our findings of *dof* for O_3 and HNO_3 are consistent with what was already assessed for IASI (e.g., [14,15]).

2.2.1.11. The observational covariance matrix. For the observation data space, we resort to the Random Projections (RP) transform (e.g., [56,59]), which also diagonalizes the observational covariance matrix, which for IASI is not diagonal because of Gaussian apodization (see e.g., [33,60]). We use inflation factors to account for possible forward model biases, whose default values can be found in [56]. The rationale of the inflation factors is to increase the observational covariance matrix, S, according to $\boldsymbol{S} = (1 + \lambda^2)\boldsymbol{S}_\varepsilon$, with $\boldsymbol{S}_\varepsilon$ the IASI observational covariance matrix, and λ a suitable scaling/inflation factor. In our scheme, λ depends on the spectral range as shown in [56]. The introduction of the inflation factors, which is largely used in spectral radiance assimilation [61], is equivalent to putting an extra smoothing constraint on the retrieval (see, e.g., [62]. For the benefit of the reader, the IASI radiometric noise and the inflation factors used to build the observational covariance matrix are shown in the supplemental material (Fig. S7 and Table S1).

3. Results

This section illustrates the results obtained with our retrieval scheme for IASI soundings recorded in 2021 and 2023. To begin with, we show the capability of the method to deal with ice polar stratospheric clouds.

3.1. Polar stratospheric clouds

According to [2] and [63], there are four accepted types of polar stratospheric clouds (PSC): NAT, type Ia, STS, type Ib or supercooled ternary solutions of nitric acid and sulfuric acid in water, ice clouds (Type II), and supercooled nitric acid (SNA) solution in water [63] has provided transmittance spectra for the four types. Our forward/inverse model can deal with ice PSCs, which can be easily detected because ice has a distinctive strong absorption at ~800 cm^{-1} and an upward peak (greater transmittance) at 1000 cm^{-1} (e.g., [63]). Given the small ice crystal dimensions, the ice absorption in the atmospheric window introduces a typical positive slope, which can be easily detected by computing the brightness temperature (BT) difference at 1000 and 800 cm^{-1} [64],

$$\Delta BT = BT_{1000} - BT_{800} \tag{15}$$

The difference is normally greater than 2 K for ice clouds. A positive slope in the atmospheric window is also a characteristic of ice tropospheric clouds. Higher ice clouds tend to give greater values of ΔBT because of the intense forward scattering of small ice crystals.

An example is shown in Fig. 5, corresponding to an IASI sounding on July 2023 at 00:00 UTC over the South Pole, −89.17° latitude, −176.76° longitude). The IASI spectrum shown in Fig. 5 has $\Delta BT \approx 10$ K. Our retrieval tool can fit the IASI spectrum and retrieve the ice water content and effective size profiles.

From Fig. 5, we see that the retrieval recovers the characteristic absorption features of ice. In particular, we can see the water ice libration band at ~12 μm, which is a recognizable absorption feature in the infrared spectrum of water ice, and is associated with water molecules' hindered rotational (librational) motions within the ice lattice [65].

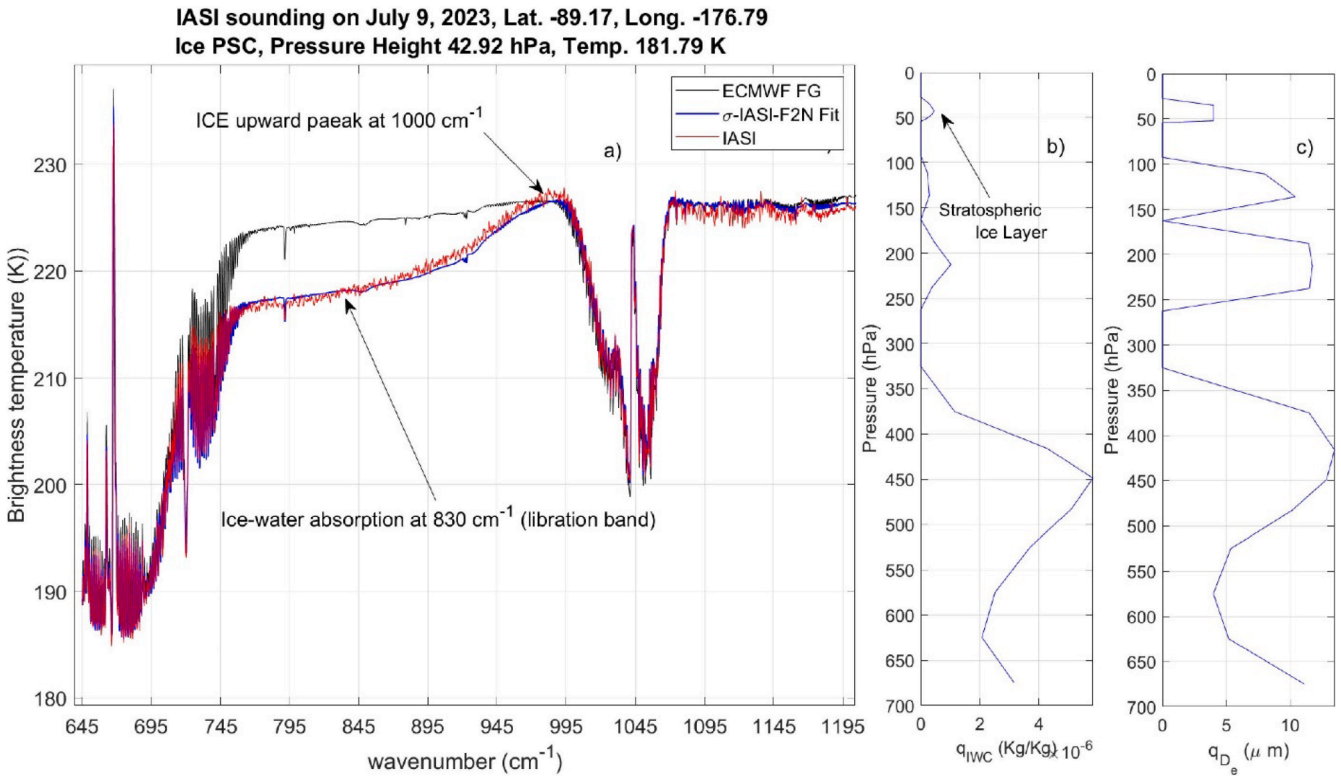

Fig. 5. Exemplifying the retrieval of a PSC type II. Panel (a) shows the first guess in black, the retrieved in blue, and the IASI spectrum in red in the spectral range 645 to 1210 cm^{-1}; panel (b) shows the retrieved , q_{IWC},profile; panel (c) shows the retrieved D_e profile. The surface pressure value is <700 hPa for the available sounding.

The retrieval of the ice mixing ratio shows an ice cloud with a complex vertical structure, with a bulk at about 450 hPa, two minor layers in the troposphere, and a layer in the stratosphere at about 43 hPa (~20 km). The temperature is ~182 K, and we note that ice clouds are supposed to exist below 188 K, which is the threshold temperature required for nucleation [2]. The mixing ratio of the ice layer in the stratosphere is 4.53 10^{-7} kg kg^{-1} (~37.2 μg/m^3), while the effective size is ~5 μm. The ice mixing ratio and the effective size we retrieve are consistent with the type of *in situ-origin* ice clouds [66]. In other words, the clouds likely originated by in situ nucleation.

The forward model does not yet include the absorption properties of NAT, type Ia, Ib; therefore, we cannot fit this type of cloud. In the hypothesis that their presence results in a signal that pops up in the residuals with an intensity above the IASI noise, the retrieval will not converge, as the forward model is not able to reproduce said feature. Conversely, if the signal is too low to be detected, the inverse system will converge, but we expect to still find a spectral signature in the residuals below the error bars, which can be evidenced by appropriate averaging. Therefore, the possible impact of NAT clouds on the IASI observations can be checked by looking at the spectral residuals in the atmospheric window 8–12 μm. The analysis of spectral residuals is shown in Section 3.3.

Fig. 5 exemplifies the potential of the forward model to deal with ice stratospheric clouds. A comprehensive analysis of the distribution and optical depths of ice stratospheric clouds requires more data and is outside the scope of this work, which focuses more on the interrelationship between O_3 and HNO_3. For brevity, maps of the liquid and ice water paths and the effective bulk size of water and ice particles have been exemplified in the supplemental material (see Fig. S8).

3.2. Ozone retrievals

As the introduction section mentions, the Copernicus Atmosphere Monitoring Service states that the last three years (2021–2023) experienced large, longer-lasting than average Southern Hemisphere ozone hole seasons. The ozone hole begins to develop in early September, in the fringe of the polar night, when the Southern Hemisphere enters the spring season (e.g., [1]). Using the IASI soundings for Sept. 9, 2021, co-registered with the four synoptic hours of the ECMWF analysis, we performed the retrieval analysis with the inversion methodology presented in the previous paragraph. ECMWF analysis are co-located with IASI soundings within $a \pm 15$ min time frame, and are used as first guess to initialize the retrieval. The ECMWF analysis also provides the first guess for ozone.

Fig. 6 shows the total ozone map as retrieved by IASI data on Sept. 9, 2021. The same Figure also compares the IASI retrieval (un-gridded level 2 product) with the co-registered ECMWF background, the TROPOMI level 2 gridded product, and the OMI level 3 gridded and smoothed product. For TROPOMI we use data with a quality flag ≥ 0.75, as suggested by the data provider (https://explore.creodias.eu/search). It is seen that neither OMI nor TROPOMI can observe the inner core of the Antarctic continent because of the polar night. Furthermore, TROPOMI does not provide data below ~−75° latitude because of cloud contamination.

Looking at Fig. 6, we conclude that the retrieved O_3 column from IASI is lower than the one from OMI, while it is much more consistent with the one from TROPOMI. It shows that the atmosphere above the inner part of the Antarctica continent has a total ozone concentration below 220 Dobson. Technically, the ozone hole forms when the total column ozone remains below 220 DU (Dobson Units). According to Krummel et al. [1], an intense polar vortex lead to a fully developed ozone hole in early September 2021.

The IASI retrieved ozone is less smooth than the gridded product delivered by OMI and TROPOMI because IASI is a level 2 product. We have not smoothed or processed it up to level 3 to demonstrate that the IASI level 2 retrieval can provide a complete picture of the spatial distribution of O_3 at the ~ 12 km scale.

To get a more quantitative assessment of the IASI product, Fig. 7

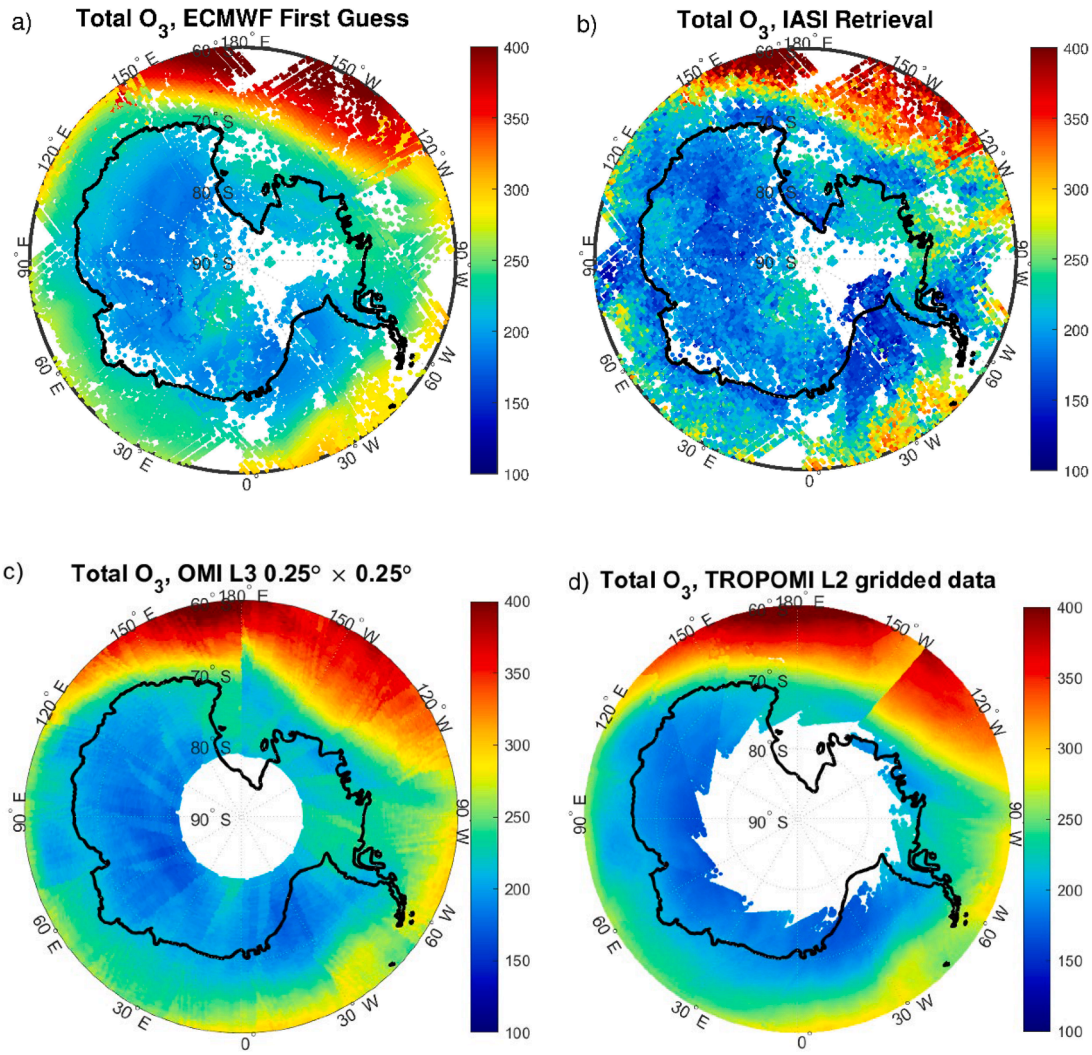

Fig. 6. Total ozone (Dobson units) analysis for the Antarctic region on Sept. 9, 2021. (a) ECMWF first guess; (b) IASI retrieval; (c) OMI L3 data; (d) TROPOMI level 2 gridded data.

shows the zonal mean computed from the data presented in Fig. 6, and the comparison with July (before the ozone hole formation) and October (when the ozone hole has fully developed). We have no data from OMI and TROPOMI for July because the Antarctic region is still in the polar night. The IASI retrieval (upper panel of Fig. 7) shows less ozone than the ECMWF analysis for the same month. The IASI-derived values are >10 % smaller than the estimated ECMWF amount from all the latitudes from −88° to −62°

On Sept. 9, 2021 (middle panel of Fig. 7), IASI and TROPOMI agree to show that the ozone hole has already formed. The OMI total column is more consistent with the ECMWF analysis, and this is likely because the OMI level 3 product is smoothed using the ECMWF data. In any case, the difference between the four data sources is well below 30 Dobson.

On Oct. 9, 2021 (lower panel of Fig. 7), ECMWF values agree with the ones derived from the three satellites and show that the ozone hole is fully formed. The relative differences are below 20 Dobson in the core of the Antarctic region. Again, we note an excellent agreement between IASI and TROPOMI.

Compared to IASI and TROPOMI, the ECMWF analysis overestimates the total ozone column. The ECMWF overestimation diminishes from winter to spring, likely because satellite data assimilation is not performed during the polar night. To our knowledge, IASI ozone is not assimilated within the ECMWF model.

We have also performed the analysis for 2023 and obtained results that are similar to those shown in Figs. 6 to 8, with the same quality as in 2021. In 2023, the ozone hole was found to be even more intense than in 2021. According to CAMS (e.g., https://atmosphere.copernicus.eu/twists-and-turns-2023-southern-hemisphere-ozone-hole) the 2023 Antarctic ozone unusually started in early August, and in September, it became the sixth-largest ozone hole ever observed. Then, it returned to average ozone hole values in October. Our analysis has shown that a large ozone-depleted air mass was already present in July, a result that is consistent with CAMS monitoring. It is thought that the erratic appearance of the ozone hole in the winter time of Antarctica is a consequence of the transport to the upper atmosphere of a large amount of water vapor because of the Hunga Tonga volcano eruption in January 2022. Recent research Evan et al. [67] has shown that volcanic aerosol and chlorine reactions trigger short-term ozone losses.

The IASI total ozone maps for Jul. 9 and Aug. 9, 2023, are shown in the Supplemental Materials for brevity (Fig. S9). Here, we limit ourselves to showing the IASI ozone retrieval analysis for September 2023, when we also have available data from OMI and TROPOMI. The total ozone is shown in Fig. 8 for the complete suite of instruments. As for the analysis of Sept. 9, 2021 (see Fig. 6), we find a good consistency with the ozone observation in the UV–VIS spectral region provided by OMI and TROPOMI. We recall that IASI is operated in the thermal infrared. Overall, our IASI level 2 data compare better with TROPOMI than OMI. OMI tends to be more coherent with the ECMWF analysis, which, as we

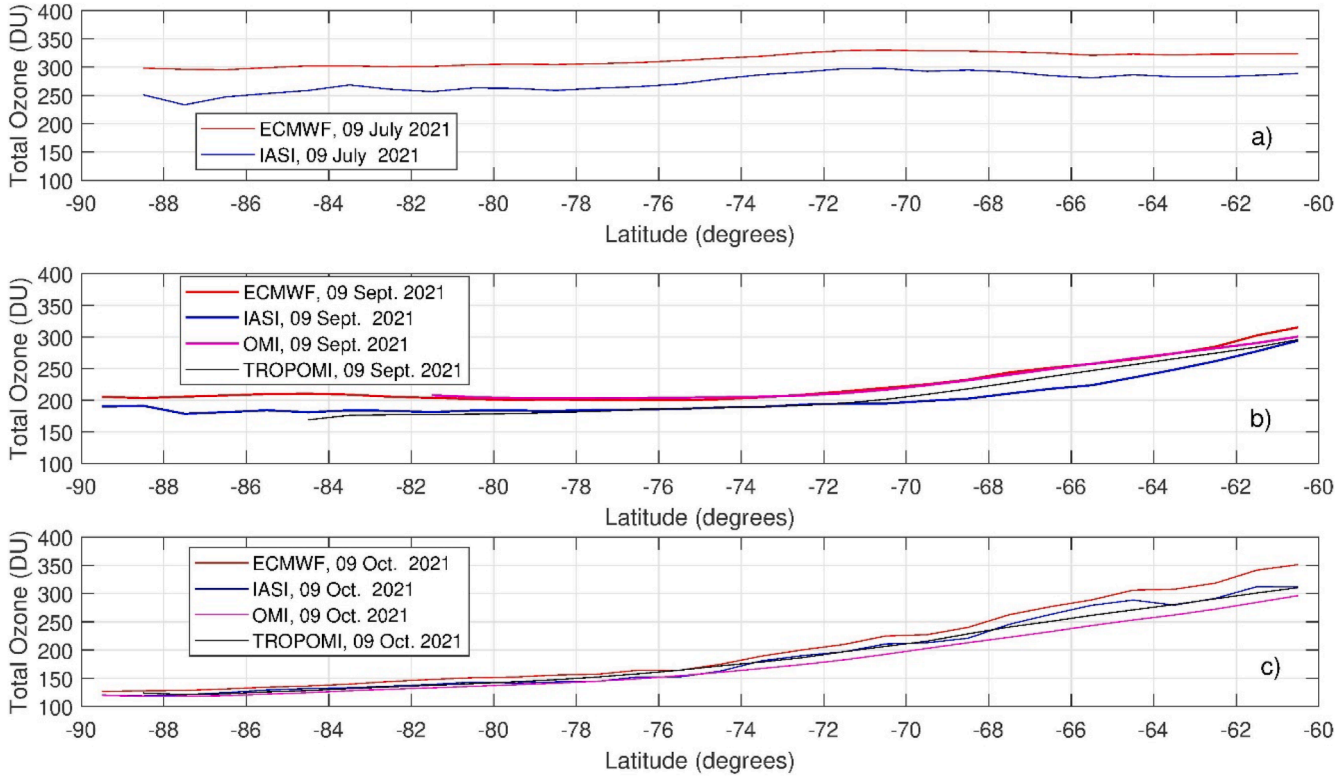

Fig. 7. Zonal mean of total ozone (Dobson units, DU) and comparison with ECMWF, OMI, and TROPOMI for different dates; (a) Jul. 9, 2021; (b) Sept. 9, 2021; (c) Oct. 9, 2021.

have already stressed, could be just the result that OMI total ozone is of the level 3 type. In effect, an inspection of OMI Level 2 data on Sept. 9, 2023, shows that the instrument recorded data on the Antarctic ocean alone (see Fig. S10 in the supplemental material), while there were no observations over the Antarctic continent, which once again stresses the importance of assimilating IASI ozone retrievals.

The good consistency between IASI and TROPOMI is also seen when we compare the zonal average (see Fig. 9) computed based on the four data sources.

It is also interesting to look at the evolution of the temperature and O_3 profiles from July to October. The temporal variation of the two parameters is shown in Fig. 10, which is obtained by averaging all IASI soundings co-registered with the ECMWF analysis at 06:00 UTC.

One interesting feature is that the temperature value at the profile minimum tends to increase while its height drops from about 15 hPa to 100 hPa. The ozone profile also undergoes dramatic changes from an almost stable mixing ratio from 100 hPa to 1 hPa (a large pressure layer) to a peaked profile with a maximum at about 10 hPa. At the same time, ozone in the lower stratosphere is heavily depleted.

We remind that the official EUMETSAT IASI level 2 system retrieves ozone only in clear sky with an Optimal Estimation approach. To highlight the improvement of sounding density when using our methodology, which is all-sky, Fig. S11 in the supplemental material shows an example of a comparison of our ozone retrieval with that officially released by EUMETSAT.

3.3. HNO_3 retrievals and inter-relationship with O_3 depletion

From Fig. 10, we see that in September, the temperature value at the profile minimum is well below the threshold of 195 K, which is the condition needed to trigger the formation of NAT. We recall that according to [2], the formation involves HNO_3 and H_2O initially in the gas phase, which then condenses into the solid phase (giving rise to crystals of HNO_3–$3H_2O$) at a temperature below 195 K. A complete spatial picture of the distributions of the HNO_3 total column, the temperature value at the minimum, and the corresponding pressure level are shown in the maps in Fig. 11.

Fig. 11 shows all the ingredients that supposedly favor the formation of PSC, in fact: (1) in the inner continent, the temperature is well below 195 K (green-yellow in Fig. 9b); (2) the pressure level at which the temperature inversion occurs in 30 to 60 hPa; (3) very low concentrations of HNO_3, below 500 pptv in the inner continent. On this aspect, it is noteworthy that our analysis suggests that PSCs formation may lead to the removal of nitric acid from the gas phase.

This is further demonstrated by Fig. 12, which analyzes the zonal averages of the total column of HNO_3 and the minimum temperature, T_{min}. The substantial depletion of the nitric acid concentration in the core of the Antarctic continent is associated with average values of T_{min} below the threshold temperature of 195 K. It is also interesting to see that the zonal average of HNO_3 vs T_{min} shows that the HNO_3 mixing ratio positively correlates with temperature up to the threshold value of 195 K (panel c), where it plateaus.

With the synergetic use of the results in Fig. 10, we conclude that NATs form possibly south of the latitude of $\sim -68°$, as we see a clear phenomenon of denitrification (e.g., Fig. 10a). From Fig. 7b, we see that in September, ozone depletion occurs below $\sim -68°$ Finally, the area below $-68°$ corresponds to the polar vortex.

The current understanding of the time evolution of the HNO_3 mixing ratio (e.g., [2,17]) places a consistent depletion of the nitric acid in the gas phase in the winter and early spring seasons of the South Pole. This behavior is believed to be consistent with the formation of NAT, which removes HNO_3 from the local environment. Our analysis of HNO_3 in July, August, and September 2023 shows this is the case (see Figs. S12 to S14 in the supplemental materials).

We think that Fig. 12 shows the most important and striking result of this study. It shows that ozone depletion is linked to denitrification of the atmosphere, which occurs at temperatures below 195 K. The result is not an artifact of the retrieval system. In effect, the correlation between

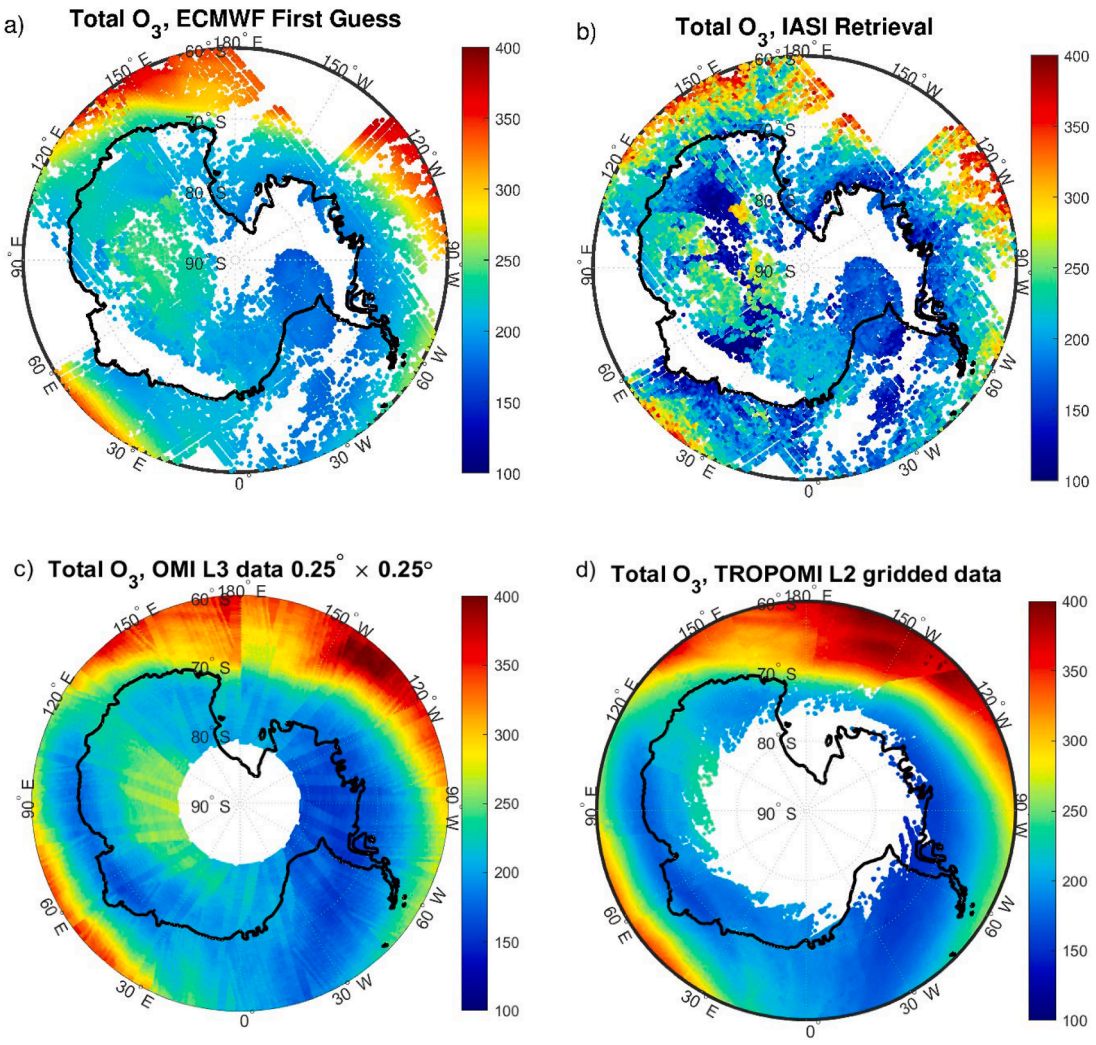

Fig. 8. Total ozone (Dobson units) analysis for the Antarctic region on Sept. 9, 2023; (a) ECMWF first guess; (b) IASI retrieval; (c) OMI L3 data; (d) TROPOMI level 2 gridded data.

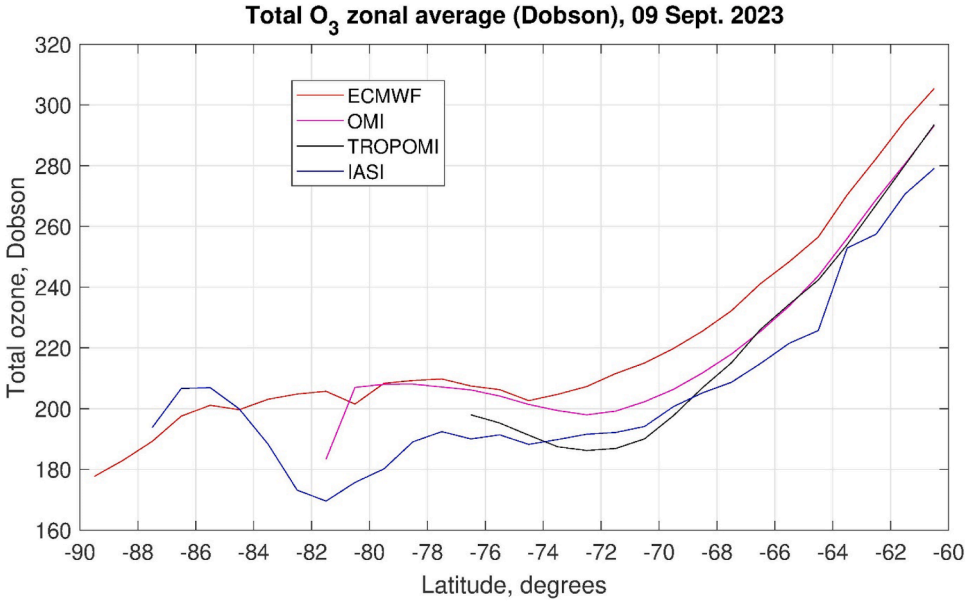

Fig. 9. Zonal mean of total ozone (Dobson units) and comparison with ECMWF, OMI, and TROPOMI for Sept. 9, 2023.

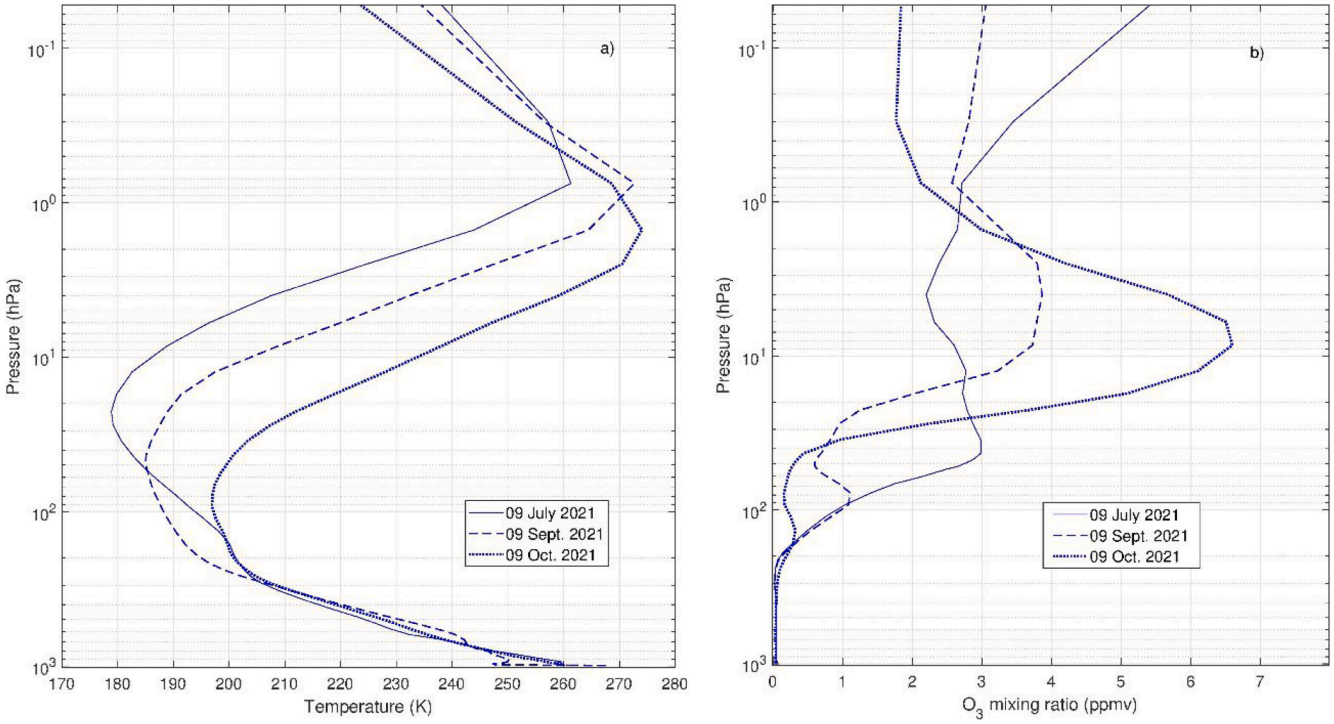

Fig. 10. Evolution of the temperature and O_3 profiles over the Antarctica region during the transition from winter to spring season. Profiles are averaged for IASI soundings at 06:00 UTC in the Southern latitude range of 60°−90°

pairs of retrievals can be checked by computing the normalized cross-covariance. For the profile pair $(T(p),\ q_{HNO_3}(p))$ the cross-correlation, *CC* is a matrix of size $N_l \times N_l$ and its elements are defined by

$$CC(i,j) = \frac{cov\left(T(i),\ q_{HNO_3}(j)\right)}{\sqrt{var(T(i))\ var\left(q_{HNO_3}(j)\right)}},\ i,j = 1,\ldots,N_l \tag{16}$$

with $X(i)$, the given parameter at pressure layer *i*-th, N_l the number of pressure layers, and where *cov* and *var* stand for covariance and variance, respectively. *CC* can be computed based on the a-posteriori covariance matrix, which is an output of the retrieval scheme. The cross-correlation can be calculated for any pair of retrievals**.** For retrievals that have been retrieved independently, the elements of *CC* need to be close to zero. Examples of the cross-correlation between the couples $(T(p),\ q_{HNO_3}(p))$ and $(O_3(p),\ q_{HNO_3}(p))$ are shown in the supplemental material (Fig. S15), and they show that the retrieval system does not introduce any correlation between any pair $(T(i),\ q_{HNO_3}(j)$, or $(O_3(i),\ q_{HNO_3}(j))$. We conclude that the results in Fig. 12 are genuinely representative of a physical-chemical process.

3.4. Spectral residuals

Analyzing spectral residuals allows us to check for possible spectroscopic inconsistency, which can reveal the presence of interfering species not modeled in our forward/inverse scheme or any spectroscopic or instrumental bias. The analysis also provides a gain in our understanding and increased confidence in the retrieval results.

In this section, we analyze the spectral residuals for the four sky/surface conditions: cloudy sky over land, clear sky over land, cloudy sky over the ocean, and clear sky over the ocean. We will use data from the IASI orbit on July 9th, 2023 at 00:00 UTC, which is still the polar night period. This choice is because, in this condition, the atmosphere experiences the coldest temperatures, which can favor the formation of stratospheric clouds and allow us to check for their spectral effects, too.

3.4.1. Cloudy sky over land spectral residuals

The cloudy sky over land is the most challenging situation because of the varying altitude and the freezing temperature in the stratosphere. Fig. 13 shows the spectral residual in the 645 to 1110 cm^{-1} range, corresponding to the longwave band 1 of the IASI instrument. This range is sensitive to the main atmospheric parameters relevant to this study: temperature, ozone, nitric acid, and stratospheric clouds. The spectral residuals shown here average over 2800 IASI soundings recorded over the Antarctic plateau. The positions of the IASI footprints for the case at hand and the other three sky/surface conditions discussed in Section 3.3 can be found in the supplemental material (Fig. S16).

With this in mind, Fig. 13 shows the spectrum computed from the ECMWF fields, the fitted IASI spectrum (top panel), and the corresponding spectral residuals (lower panel) computed as the difference between observed and calculated spectra (Obs-Calc) at the end of the inversion process. The ECMWF spectrum is computed based on the co-registered ECMWF state vector, which we use as a first guess. The fitted spectrum is computed based on the retrieved state vector.

It is seen that the ECMWF yields a spectrum warmer than the IASI observations. Upon retrieval, the calculations fit within the error bars of the IASI observations over the whole spectral range. The IASI error bars have been converted to units of brightness temperature or NEDT, which depends on the scene temperature and increases as the temperature decreases. The IASI noise used in the analysis is released by EUMETSAT (e.g., [60]). It has been adequately inflated to consider possible forward model biases (e.g., [23]).

The spectral residual in Fig. 13 shows that the retrieval system fits the IASI spectra within the error bars, and, therefore, the retrieval product is consistent with the observations. From Fig. 13, the Obs-FG residuals show HDO spikes in the 1100 to 1200 cm^{-1} range, which are removed when we perform the inversion of the spectral radiances, meaning that the proper concentration of HDO is retrieved. A good fit is also seen for the CO_2 absorption band, although a spectral signature is still seen, which is within the noise bars. The CO_2 feature corresponding to the Q-branch of CO_2 at ~791 cm^{-1} is seen in absorption in the first guess spectrum, whereas it appears in emission in the IASI spectrum.

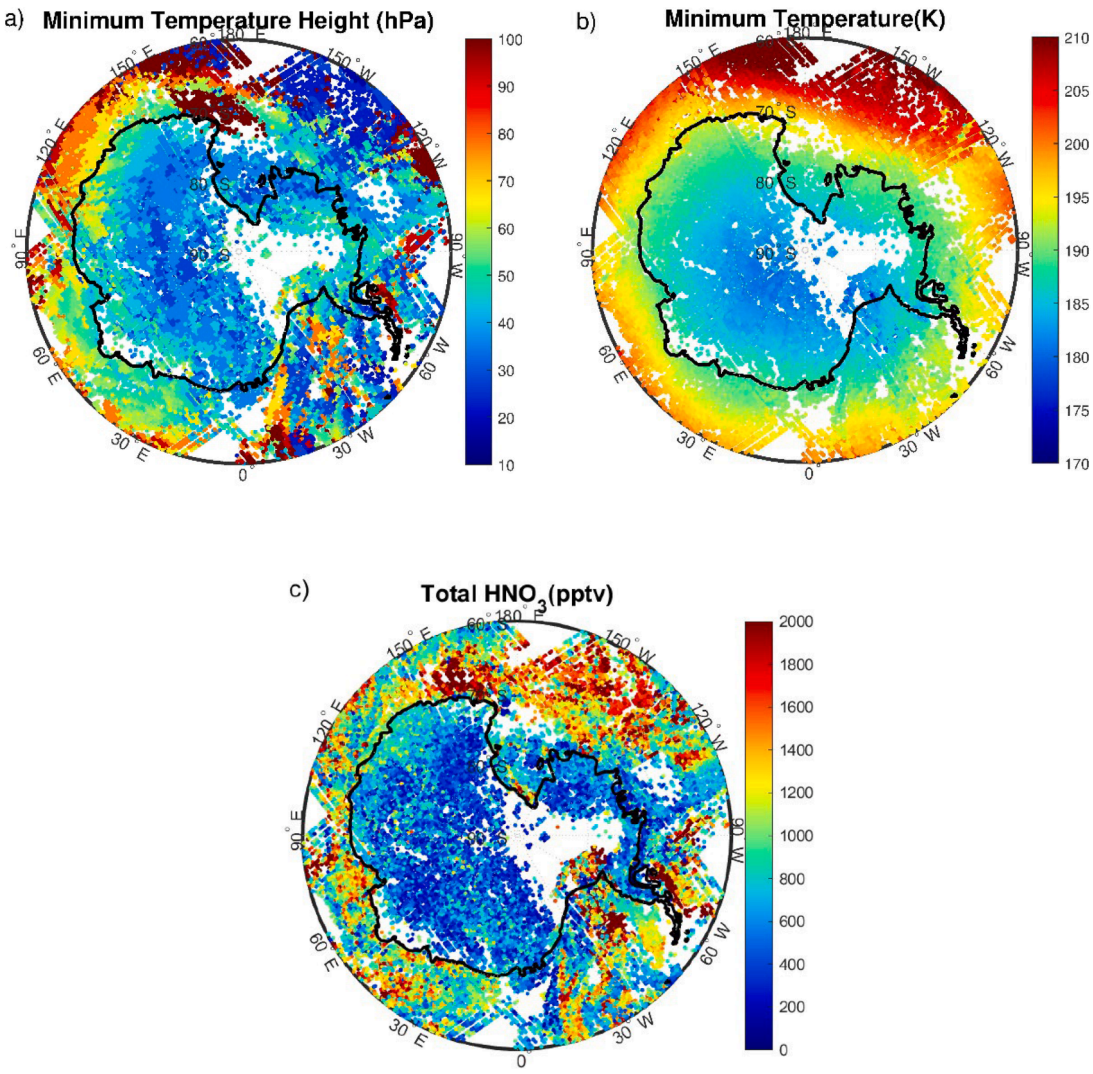

Fig. 11. IASI retrieval analysis for the Antarctic region on Sept. 9, 2021. (a) the Pressure level at which the temperature profile gets its minimum; (b) the temperature at the minimum (T_{min}), and (c) the total column of HNO_3.

Upon retrieval, the modeled feature appears in emission, net of a small residual within error bars. It should be noted that the water vapor lines in the same region appear consistently in emission. We also note that the ozone band is fitted with a spectral residual close to zero, whereas it appears much deeper when using ECMWF analyses. This is consistent with the already noted difference between OMI L3 ozone and the one retrieved using IASI data, which is consistently lower.

Although within the noise bars, we also see an evident signature in the window spectral range 800 to 900 cm^{-1}, where the observed BT appears colder than the computed one by about ~ 0.5 K. It is important to stress that we do not see sharp spectral features, rather a continuum, which could be consistent with an aerosol-like absorption not modeled in our forward radiative transfer. It is reasonable to think that this slight bias could be due to undetected and unrepresented stratospheric clouds.

3.4.2. *Clear sky over land spectral residuals*

The spectral residuals over land in clear sky allow us to gain confidence in the hypothesis further if the broad signature seen in the range 800 to 900 cm^{-1} in Fig. 13 can be attributed to clouds. The spectral residuals shown in Fig. 14 confirm this, and it is soon evident that the broad absorption signature disappears in the clear sky; therefore, it is not a model artifact when it is rather a real feature in the cloudy atmosphere. The spectra shown in Fig. 14 are based on 977 IASI soundings. It is also interesting to see that the ECMWF ozone analysis in clear sky is quite close to the real IASI observations. However, a relatively large misfit exists for the temperature profile, as it is possible to see from the residuals in the CO_2 absorption band. Finally, we consistently retrieve emissivity in the clear sky over land (see Fig. S17 in the supplemental material).

A comparison of Fig. 13 vs. Fig. 14 allows us to say that the spectral residuals in the range 800–900 cm^{-1} are most likely related to the impact of stratospheric clouds.

The large misfit of the ECMWF FG in the CO_2 tropospheric channels seen in Fig. 14 deserves attention. Our analysis suggests that the misfit results from an incorrect first-guess temperature profile. However, it might also result from an improper CO_2 profile. Temperature is derived from the CO_2 absorption band, and upon retrieval, the temperature estimate could be biased to compensate for a supposedly wrong CO_2 profile. However, this is not the case in our scheme because CO_2 is simultaneously retrieved with temperature. As described in Section 2.2.1.4, temperature and CO_2 retrievals do not insist on using the same channels. A comprehensive check of the retrievals for CO_2 and temperature for the IASI soundings on July 9, 2023, which includes the comparison of the temperature retrieved profiles against those of the ECMWF Fist Guess, retrieved CO_2 against First Guess CO_2, the cross-correlation of the retrieved Temperature and CO_2, and, finally, the

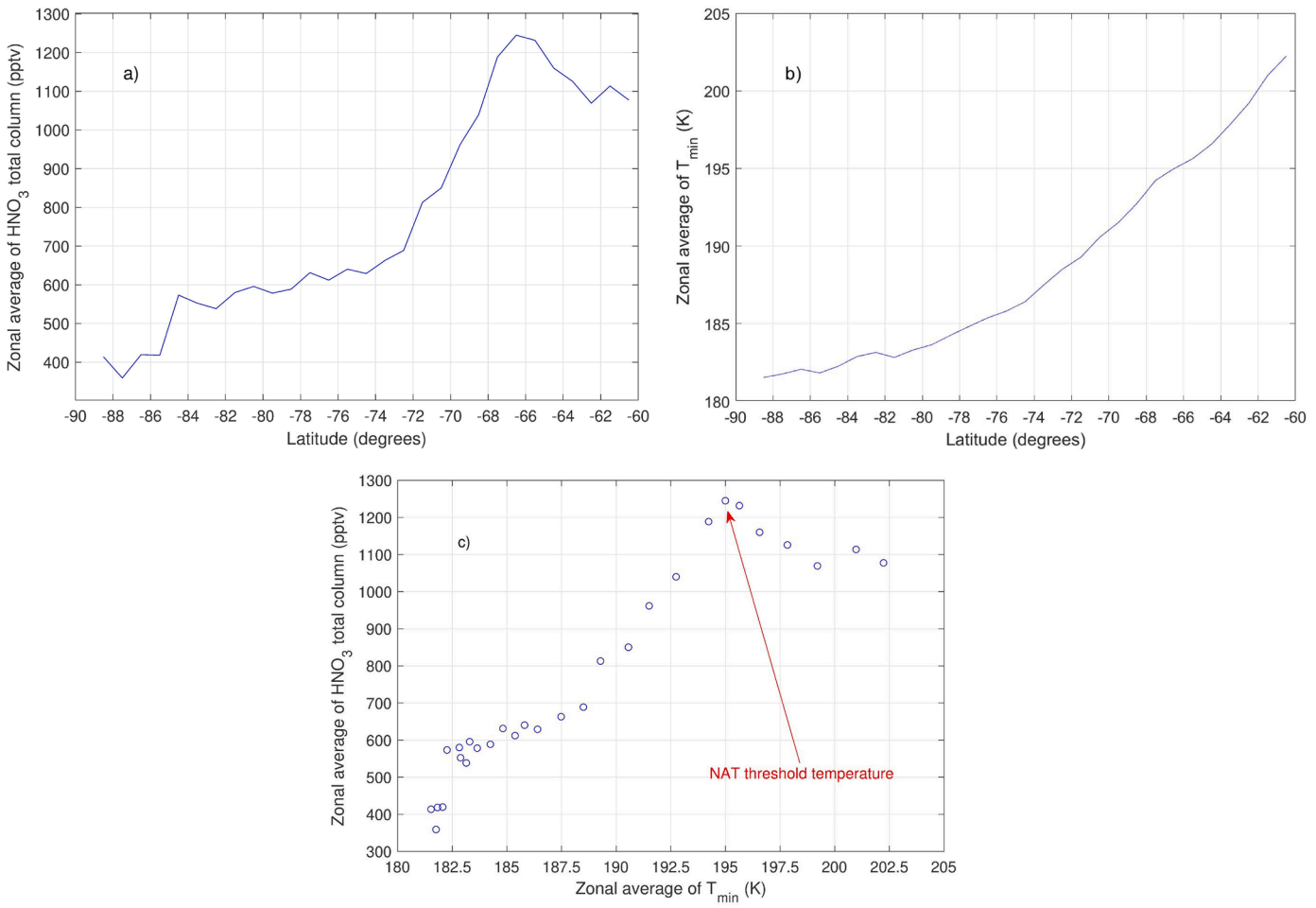

Fig. 12. (a) Zonal mean of total HNO_3 (pptv); (b) zonal mean of T_{min}; (c) scatter plot of the data shown in (a) and (b). From panel (c), it is possible to note that HNO_3 increases with temperature up to the threshold value of 195 K. Zonal averages have been obtained using the data shown in Fig. 11.

standard deviation of the spectral residuals, is provided in the supplemental material (Figs. S18 to S22). It is also important to stress that the first guess and the IASI retrieval for XCO_2 are consistent with the in situ concentration of CO_2 as measured at the South Pole Observatory (site latitude: $-89.98°$, longitude: $-24.8°$, 2810.0 m). The SPO monthly mean for July 2023 is 416.7 ppmv (https://gml.noaa.gov/dv/data/index.php?site=SPO), whereas the average value for XCO_2 corresponding to the 977 soundings in Fig. 14 is 411.5 for the First Guess and 417.0 ppmv upon retrieval: neither the first guess nor the retrieval shows any anomaly concerning the CO_2 concentration. Finally, we stress that a difference of ± 10 ppmv of the assumed profile against the actual CO_2 profile would affect the retrieval of the temperature of less than ± 0.5 K at any pressure level [68]. Therefore, unless we claim a CO_2 hole in Antarctica, in addition to that of ozone, the misfit seen in Fig. 14 is mainly due to temperature and gives evidence of how our scheme can also add information to the temperature retrieval.

3.4.3. *Cloudy sky over ocean spectral residuals*

Another important check comes from analyzing the spectral residuals in cloudy conditions over the ocean. Stratospheric clouds are rare over the ocean because of the warmer stratosphere as compared to the atmosphere over cold land surfaces, such as over the Antarctica continent. The spectral residuals in Fig. 15 do not show any systematic effect in the atmospheric window, where the residual is nearly zero. The analysis shown in Fig. 15 is based on 1414 IASI soundings.

We also note that, compared with Fig. 13, we have some discrepancies in the tropospheric absorption portion of the CO_2 absorption band. This is because the IASI observations are less sensitive to the lower atmosphere in the cloudy sky. The residuals in the CO_2 ν_2 band show a similar pattern to those in Fig. 13 for cloudy sky over land. Compared to the residuals shown for land, it is important to point out (here and in the following case) that HNO_3 residual misfits (spikes) are also visible, particularly in the Q-branch at 878 cm^{-1}. This misfit is well visible in the ECMWF residuals, while it falls within IASI error bars upon retrieval. The fact that, upon fitting, this spectral misfit is unnoticeable in the residuals over land and sea also testifies to the good HNO_3 retrieval at the southernmost latitudes.

3.4.4. *Clear sky over ocean spectral residuals*

Clear sky cases over the ocean at latitudes lower than $-60°$ are rare. In fact, over the ocean, we have almost always cloudy conditions (see supplemental material). For the spectral residuals in Fig. 16, we had only 137 IASI soundings, which are still enough to produce a significant residual analysis.

As expected, the spectral residuals fall within the error bars everywhere in the spectral range, and we cannot see any systematic and significant behavior. As for the case of clear sky over land, the CO_2 is well-fitted because the IASI observations can "see" the lower atmosphere. Also, it should be noted that the temperature in the atmospheric window is well below 273 K. The soundings are over sea ice rather than seawater, as testified by the surface temperature retrieval that yields values below 273 K. The fact that the surface is sea ice also explains some slight systematic patterns in the residuals. In effect, we set the emissivity to that of seawater, and, unlike the land surface case, it is not

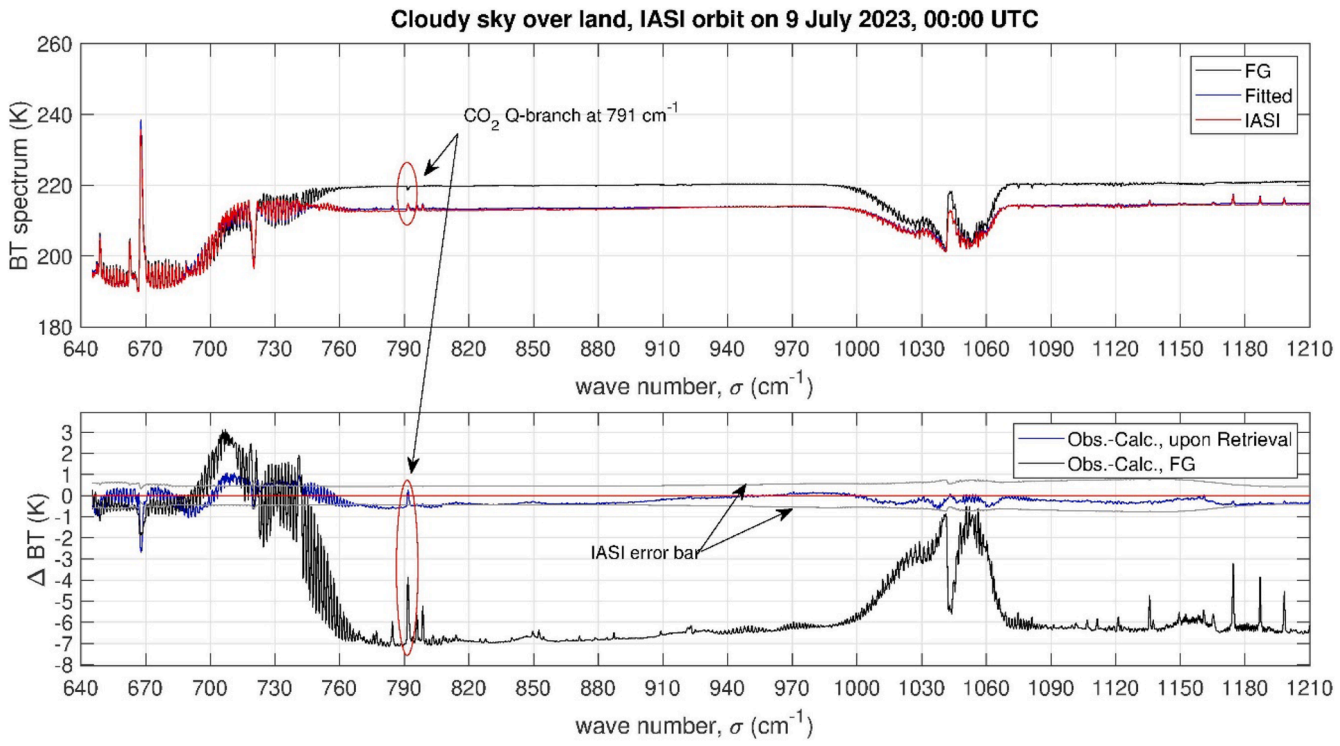

Fig. 13. Average spectrum computed from the ECMWF fields, average observed IASI spectrum, and fitted average spectrum (top panel) together with spectral residuals (bottom panel) in IASI band 1 based on the retrieval analysis of the IASI soundings on July 9, 2023. The red circles in Figure refer to the CO_2 spectral line features at 791 cm^{-1}. The spectra average over 2800 land surface, with cloudy sky IASI soundings.

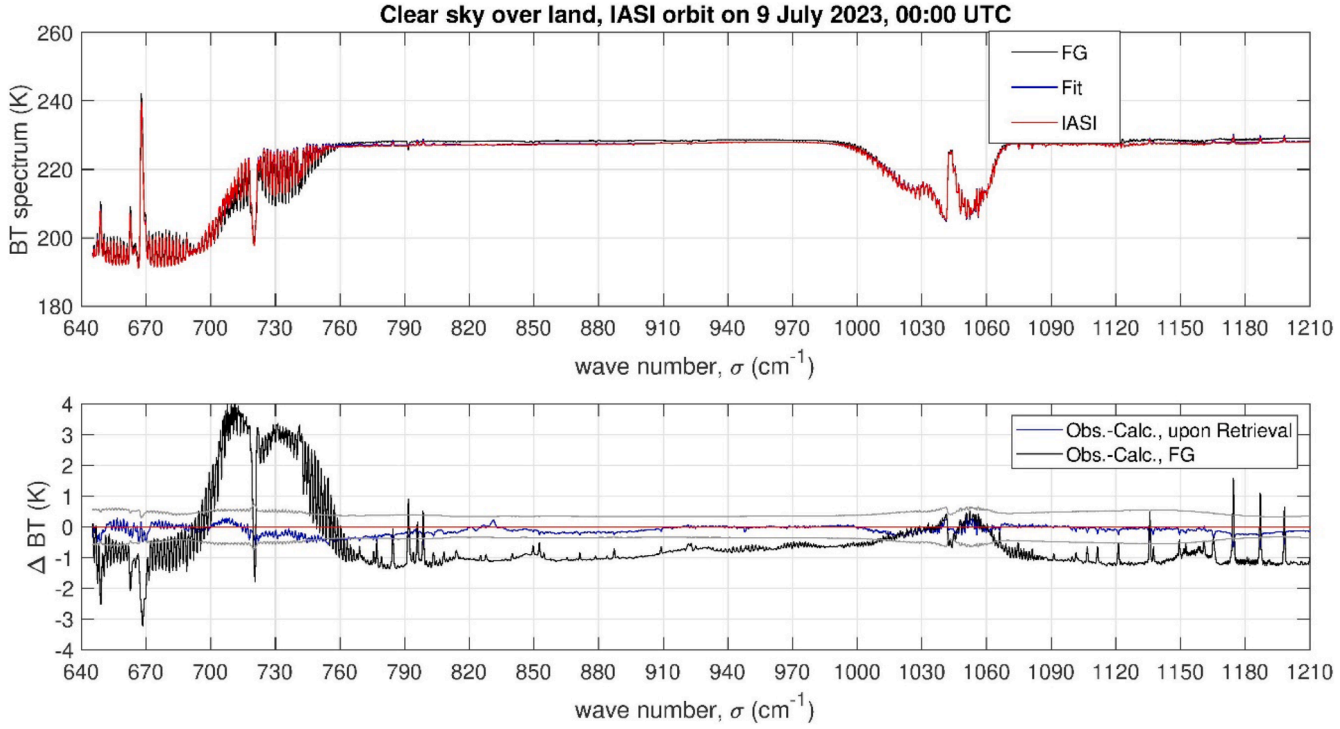

Fig. 14. Average spectrum computed from the ECMWF fields, average observed IASI spectrum, and fitted average spectrum (top panel) together with spectral residual (bottom panel) in IASI band 1 based on the retrieval analysis of IASI soundings on July 9, 2023. The spectra average over 977 footprints over land in clear sky conditions.

retrieved. The patterns are likely due to the emissivity properties of the surface. However, it should be stressed that the error bars in the atmospheric window are within ±0.3 K.

Fig. 16 also evidences two spike features (circled in magenta on the black line in the bottom panel) in the FG spectral residuals at ~879.0 and ~896.5 cm^{-1}. These features are due to the ν_5 and $2\nu_9$ cold bands of

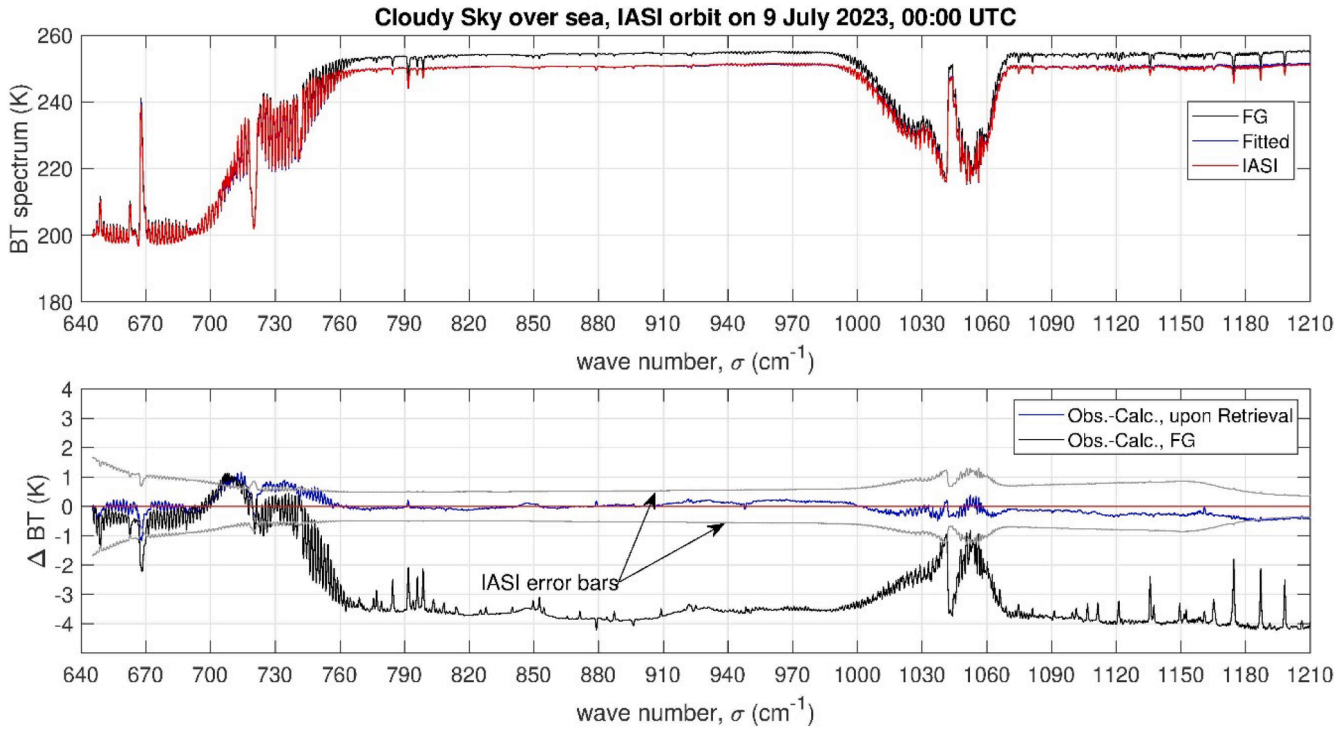

Fig. 15. Average spectrum computed from the ECMWF fields, average observed IASI spectrum, and fitted average spectrum (top panel) together with spectral residual (bottom panel) in IASI band 1 based on the retrieval analysis of the IASI soundings on July 9, 2023. The spectra are averaged over 1414 footprints over the sea in cloudy conditions.

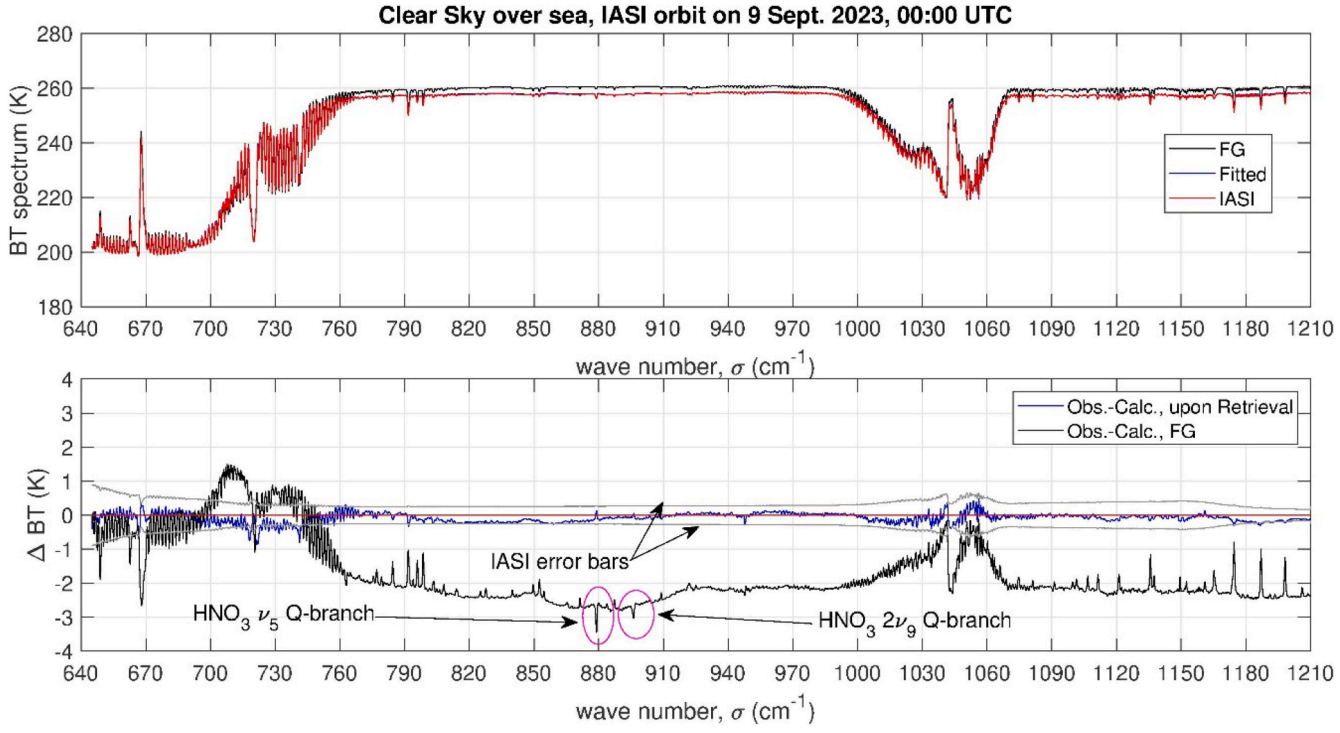

Fig. 16. Average spectrum computed from the ECMWF fields, average observed IASI spectrum, and fitted average spectrum (top panel) together with spectral residuals (bottom panel) in IASI band 1 based on the retrieval analysis of the IASI soundings on July 9, 2023. The magenta circles in the FG spectral residual evidence HNO_3 spectral line features. The spectra average over 137 footprints over the sea surface in clear sky conditions.

HNO_3, respectively. Both features are largely attenuated upon fitting, which exemplifies how our retrieval for HNO_3 is consistent with the observations. For brevity, the details of the spectral range 860 to 905 cm^{-1} of Fig. 16 are zoomed in Fig. S23 of the supplemental material.

In the window region 800–1200 cm^{-1}, the spectral residual corresponding to the first guess shows line features that appear mostly flipped

up (mainly lines of H_2O, HDO, and CO_2), meaning that the IASI observations show less absorption than the first guess. Conversely, the fact that the HNO_3 line features are flipped down means that IASI shows more absorption than the first guess. The HNO_3 (flipped down) spectral features can also be seen in the FG average spectrum in the cloudy sky over the sea (see Fig. 15). In contrast, they almost disappear in the case of the land surface (see Figs. 13 and 14). The reason is that the FG total amount of HNO_3 is $\sim$ 500 pptv, and this value turns out to be essentially different from the values we effectively retrieve over the sea and closer to those estimated for land (see, e.g., Fig. S1 in the supplemental material).

4. Conclusions and outlook

We have presented an all/sky forward/inverse tool and demonstrated its capability by analyzing the onset of the Antarctica ozone hole in 2021 and 2023. The study used all/sky IASI spectra recorded over the latitude range -60° to -90° for the winter/spring months. The analysis shows that ozone depletion begins in the fringe of the polar night. Nitric acid has been detected and quantified in the gas phase. The area of depleted ozone extends from 90° to ~70° Southern latitudes. We have shown that the temperature profile has an inversion at a pressure level that can be as high as 10 hPa; the minimum temperature is below the threshold of 195 K, which is needed for NAT formation. The analysis indicates a possible formation of such clouds at altitudes between 20 km and 35 km. The ozone depletion parallels a significant decrease of HNO_3 in the gas phase, and the regions where we see this effect are characterized by a minimum stratospheric temperature below the threshold of 195 K. This supports the idea that nitric acid condenses, supposedly giving rise to crystals of HNO_3–$3H_2O$. The observational connection between clouds, HNO_3, and ozone in IASI data is one of the most significant results of the study conducted in this paper.

We have shown that spectral observations can consistently retrieve ozone, nitric acid, water, and ice clouds. Spectral residuals are usually reduced within the noise error bars, regardless of sky conditions and surface types. Stratospheric ice cloud spectral features are fitted within NEDT, showing that the state-of-the-art spectroscopy of ice particles is good enough for retrieval analysis. More work needs to be done to have a more comprehensive assessment of all PSC types.

We have also evidenced the presence of ice stratospheric clouds at temperatures below 188 K. Ice clouds have strong absorption in the atmospheric window in the range 800–1000 cm^{-1} and can be detected. The analysis of the residuals of cloudy spectra over the Antarctic plateau shows an excess absorption in the spectral domain 800–900 cm^{-1}, which could be attributed to some undetected NAT clouds.

We have found that in 2023, the ozone hole was more profound and extended than it was in 2021. Air masses of depleted ozone were found in July and August when the Antarctica continent was still in the polar night. An analysis of the spectral residuals shows that the ozone retrieval is fully consistent with the IASI observations. The deeper ozone depletion in 2023 could result from interaction with the Hunga Tonga volcano eruption in January 2022 [67].

There are at least three points where our strategy can have some advantages (and not only limited to the Antarctica case study):

1. Enable the use of cloudy radiances in the infrared and characterize liquid and ice clouds along with thermodynamical parameters and minor and trace gases. This feature has been exemplified in Fig. 5, where we show the detection and analysis of a stratospheric ice cloud.
2. Work with all-sky conditions (clear and cloudy), improving retrievals' horizontal spatial and temporal sampling. This feature has been exemplified, e.g., in Fig. 10 where zonal averages at a latitude resolution of 1° of the many parameters we retrieve allow us to assess that the ozone depletion area corresponds to a zone of strong denitrification.
3. Maximize daily coverage by analyzing day and night soundings and providing, e.g., valid retrievals during the polar night. Retrievals have exemplified this feature in the southern winter months of July and August.

Our work is not intended and cannot be an exhaustive analysis of the ozone hole. It is a first step in developing a methodology for retrievals in all-sky conditions. Its application to the Southern Hemisphere ozone hole exemplifies how the approach can add new information to previous studies. Furthermore, it shows the importance of assimilating all-sky infrared radiances. We have proven that IASI spectra can lead to valid and interesting retrievals during the polar night and early spring when UV–VIS satellite observations are not possible.

Authors statement

Authors have nothing to disclose, therefore we do not add any statement.

CRediT authorship contribution statement

Carmine Serio: Writing – original draft, Methodology, Formal analysis, Conceptualization. **Guido Masiello:** Software, Methodology, Data curation. **Giuliano Liuzzi:** Writing – review & editing, Software, Formal analysis. **Angela Cersosimo:** Resources, Data curation. **Tiziano Maestri:** Writing – review & editing, Methodology, Funding acquisition. **Michele Martinazzo:** Validation, Software. **Fabrizio Masin:** Visualization, Software, Data curation. **Giorgia Proietti Pelliccia:** Validation, Data curation. **Sara Venafra:** Software. **Claude Camy-Peyret:** Writing – review & editing, Supervision.

Declaration of competing interest

The authors declare that they have no known competing financial interests or personal relationships that could have appeared to influence the work reported in this paper.

Data availability

Data will be made available on request.

Acknowledgments

OMI data used in this paper were downloaded from the NASA EARTHDATA website https://www.earthdata.nasa.gov/learn/find-data/near-real-time/omi. We acknowledge OMI data are provided by NASAs Distributed Active Archive Centers (DAACs), which are parts of NASAs Earth Observing System Data and Information System (EOSDIS) managed by NASAs Earth Science Data and Information System (ESDIS) Project. TROPOMI data have been downloaded from the website https://explore.creodias.eu/search. We acknowledge TROPOMI data are provided by the CAM system, https://atmosphere.copernicus.eu/. We also acknoweledge background and first guess data as shown in Table 2 are provided by the ECMWF ecgate service, CAMS ECG4, and CAMS *global atmospheric composition forecasts* systems.

IASI has been developed and built under the responsibility of the Centre National d'Etudes Spatiales (CNES, France). It is onboard the Metop satellites as part of the EUMETSAT Polar System. The IASI L1C data are received through the EUMETCast near real-time data distribution service. This research was carried out in the framework of the projects FORUM-Scienza (contract n-2018–6-Q.0, consortium led by CNR-INO Florence) and Fit-FORUM (contract n. 2023–23-HH.0, consortium led by DIFA, University of Bologna), which the Italian Space Agency funded.

Supplementary materials

Supplementary material associated with this article can be found, in the online version, at doi:10.1016/j.jqsrt.2024.109211.

References

[1] Krummel PB, Fraser PJ, Derek N. The 2021 Antarctic Ozone Hole Summary: Final Report. Report prepared for the Australian Government Department of Agriculture, Water and the Environment. Australia: CSIRO; 2022. p. 30.

[2] Tritscher I, Pitts MC, Poole LR, Alexander SP, Cairo F, Chipperfield MP, Grooß J-U, Höpfner M, Lambert A, Luo B, Molleker S, Orr A, Salawitch R, Snels M, Spang R, Woiwode W, Peter T. Polar stratospheric clouds: satellite observations, processes, and role in ozone depletion. Rev Geophys 2021;59:e2020RG000702. https://doi.org/10.1029/2020RG000702.

[3] Spang R, Remedios JJ. Observations of a distinctive infra-red spectral feature in the atmospheric spectra of polar stratospheric clouds measured by the CRISTA instrument. Geophys Res Lett 2003;30. https://doi.org/10.1029/2003GL017231.

[4] Spang R, Hoffmann L, Höpfner M, Griessbach S, Müller R, Pitts MC, Orr AMW, Riese M. A multi-wavelength classification method for polar stratospheric cloud types using infrared limb spectra. Atmosph Meas Tech 2016;9:3619–39. https://doi.org/10.5194/amt-9-3619-2016.

[5] Höpfner M, Deshler T, Pitts M, Poole L, Spang R, Stiller G, von Clarmann T. The MIPAS/Envisat climatology (2002–2012) of polar stratospheric cloud volume density profiles. Atmosph Meas Tech 2018;11:5901–23. https://doi.org/10.5194/amt-11-5901-2018.

[6] Pitts MC, Thomason LW, Poole LR, Winker DM. Characterization of polar stratospheric clouds with spaceborne lidar: CALIPSO and the 2006 Antarctic season. Atmosph Chem Phys 2007;7:5207–28. https://doi.org/10.5194/acp-7-5207-2007.

[7] Pitts MC, Poole LR, Thomason LW. CALIPSO polar stratospheric cloud observations: second-generation detection algorithm and composition discrimination. Atmosph Chem Phys 2009;9:7577–89. https://doi.org/10.5194/acp-9-7577-2009.

[8] Pitts MC, Poole LR, Dörnbrack A, Thomason LW. The 2009–2010 arctic polar stratospheric cloud season: a CALIPSO perspective. Atmosph Chem Phys 2011;11:2161–77. https://doi.org/10.5194/acp-11-2161-2011.

[9] Pitts MC, Poole LR, Lambert A, Thomason LW. An assessment of CALIOP polar stratospheric cloud composition classification. Atmosph Chem Phys 2013;13:2975–88. https://doi.org/10.5194/acp-13-2975-2013.

[10] Pitts MC, Poole LR, Gonzalez R. Polar stratospheric cloud climatology based on CALIPSO spaceborne lidar measurements from 2006 to 2017. Atmosph Chem Phys 2018;18:10881–913. https://doi.org/10.5194/acp-18-10881-2018.

[11] Waters JW, Froidevaux L, Harwood RS, Jarnot RF, Pickett HM, Read WG, Siegel PH, Cofield RE, Filipiak MJ, Flower DA, Holden JR, Lau GK, Livesey NJ, Manney GL, Pumphrey HC, Santee ML, Wu DL, Cuddy DT, Lay RR, Loo MS, Perun VS, Schwartz MJ, Stek PC, Thurstans RP, Boyles MA, Chandra KM, Chavez MC, Chen G-S, Chudasama BV, Dodge R, Fuller RA, Girard MA, Jiang JH, Jiang Y, Knosp BW, LaBelle RC, Lam JC, Lee KA, Miller D, Oswald JE, Patel NC, Pukala DM, Quintero O, Scaff DM, Van Snyder W, Tope MC, Wagner PA, Walch MJ. The Earth observing system microwave limb sounder (EOS MLS) on the aura Satellite. IEEE Trans Geosci Remote Sens 2006;44:1075–92. https://doi.org/10.1109/TGRS.2006.873771.

[12] Schwartz MJ, Lambert A, Manney GL, Read WG, Livesey NJ, Froidevaux L, Ao CO, Bernath PF, Boone CD, Cofield RE, Daffer WH, Drouin BJ, Fetzer EJ, Fuller RA, Jarnot RF, Jiang JH, Jiang YB, Knosp BW, Krüger K, Li J-LF, Mlynczak MG, Pawson S, Russell III JM, Santee ML, Snyder WV, Stek PC, Thurstans RP, Tompkins AM, Wagner PA, Walker KA, Waters JW, Wu DL. Validation of the Aura Microwave Limb Sounder temperature and geopotential height measurements. J Geophys Res Atmosph 2008;113. https://doi.org/10.1029/2007JD008783.

[13] Hilton F, Armante R, August T, Barnet C, Bouchard A, Camy-Peyret C, Capelle V, Clarisse L, Clerbaux C, Coheur P-F, Collard A, Crevoisier C, Dufour G, Edwards D, Faijan F, Fourrié N, Gambacorta A, Goldberg M, Guidard V, Hurtmans D, Illingworth S, Jacquinet-Husson N, Kerzenmacher T, Klaes D, Lavanant L, Masiello G, Matricardi M, McNally A, Newman S, Pavelin E, Payan S, Péquignot E, Peyridieu S, Phulpin T, Remedios J, Schlüssel P, Serio C, Strow L, Stubenrauch C, Taylor J, Tobin D, Wolf W, Zhou D. Hyperspectral earth observation from IASI: five years of accomplishments. Bull Am Meteorol Soc 2012;93:347–70. https://doi.org/10.1175/BAMS-D-11-00027.1.

[14] Wespes C, Hurtmans D, Clerbaux C, Santee ML, Martin RV, Coheur PF. Global distributions of nitric acid from IASI/MetOP measurements. Atmosph Chem Phys 2009;9:7949–62. https://doi.org/10.5194/acp-9-7949-2009.

[15] Hurtmans D, Coheur P-F, Wespes C, Clarisse L, Scharf O, Clerbaux C, Hadji-Lazaro J, George M, Turquety S. FORLI radiative transfer and retrieval code for IASI. J Quant Spectrosc Radiat Transf 2012;113:1391–408. https://doi.org/10.1016/j.jqsrt.2012.02.036. Three Leaders in Spectroscopy.

[16] Ronsmans G, Langerock B, Wespes C, Hannigan JW, Hase F, Kerzenmacher T, Mahieu E, Schneider M, Smale D, Hurtmans D, De Mazière M, Clerbaux C, Coheur P-F. First characterization and validation of FORLI-HNO_3 vertical profiles retrieved from IASI/Metop. Atmosph Meas Tech 2016;9:4783–801. https://doi.org/10.5194/amt-9-4783-2016.

[17] Wespes C, Ronsmans G, Clarisse L, Solomon S, Hurtmans D, Clerbaux C, Coheur P-F. Polar stratospheric nitric acid depletion surveyed from a decadal dataset of IASI total columns. Atmosph Chem Phys 2022;22:10993–1007. https://doi.org/10.5194/acp-22-10993-2022.

[18] Tang G, Yang P, Kattawar GW, Huang X, Mlawer EJ, Baum BA, King MD. Improvement of the simulation of cloud longwave scattering in broadband radiative transfer models. J Atmosph Sci 2018;75:2217–33. https://doi.org/10.1175/JAS-D-18-0014.1.

[19] Martinazzo M, Magurno D, Cossich W, Serio C, Masiello G, Maestri T. Assessment of the accuracy of scaling methods for radiance simulations at far and mid infrared wavelengths. J Quant Spectrosc Radiat Transf 2021;271:107739. https://doi.org/10.1016/j.jqsrt.2021.107739.

[20] Masiello G, Serio C, Maestri T, Martinazzo M, Masin F, Liuzzi G, Venafra S. The new σ-IASI code for all sky radiative transfer calculations in the spectral range 10 to 2760 cm-1: σ-IASI/F2N. J Quant Spectrosc Radiat Transf 2024;312:108814. https://doi.org/10.1016/j.jqsrt.2023.108814.

[21] Chou M-D, Lee K-T, Tsay S-C, Fu Q. Parameterization for cloud longwave scattering for use in atmospheric models. J Clim 1999;12:159–69. https://doi.org/10.1175/1520-0442(1999)012<0159:PFCLSF>2.0.CO;2.

[22] Rodgers CD. Inverse methods for atmospheric sounding: theory and practice. World Scientific; 2000. https://doi.org/10.1142/3171.

[23] Liuzzi G, Masiello G, Serio C, Venafra S, Camy-Peyret C. Physical inversion of the full IASI spectra: assessment of atmospheric parameters retrievals, consistency of spectroscopy and forward modelling. J Quant Spectrosc Radiat Transf 2016;182:128–57. https://doi.org/10.1016/j.jqsrt.2016.05.022.

[24] Serio C, Masiello G, Camy-Peyret C, Liuzzi G. CO2 spectroscopy and forward/inverse radiative transfer modelling in the thermal band using IASI spectra. J Quant Spectrosc Radiat Transf 2019;222-223:65–83. https://doi.org/10.1016/j.jqsrt.2018.10.020.

[25] DeSouza-Machado S, Strow LL, Tangborn A, Huang X, Chen X, Liu X, Wu W, Yang Q. Single-footprint retrievals for AIRS using a fast Two Slab cloud-representation model and the SARTA all-sky infrared radiative transfer algorithm. Atmospheric Meas Tech 2018;11:529–50. https://doi.org/10.5194/amt-11-529-2018.

[26] Zhou, D.K., Smith, W.L., Liu, X., Larar, A.M., Mango, S.A., Huang, H.-L., 2007. Physically retrieving cloud and thermodynamic parameters from ultraspectral IR measurements. 10.1175/JAS3877.1.

[27] Zhou DK, Smith WL, Larar AM, Liu X, Taylor JP, Schlüssel P, Strow LL, Mango SA. All weather IASI single field-of-view retrievals: case study – validation with JAIVEx data. Atmosph Chem Phys 2009;9:2241–55. https://doi.org/10.5194/acp-9-2241-2009.

[28] Liu X, Yang Q, Li H, Jin Z, Wu W, Kizer S, Zhou DK, Yang P. Development of a fast and accurate PCRTM radiative transfer model in the solar spectral region. Appl Opt 2016;55:8236–47. https://doi.org/10.1364/AO.55.008236.

[29] Wu W, Liu X, Zhou DK, Larar AM, Yang Q, Kizer SH, Liu Q. The application of PCRTM physical retrieval methodology for IASI cloudy scene analysis. IEEE Trans Geosci Remote Sens 2017;55:5042–56. https://doi.org/10.1109/TGRS.2017.2702006.

[30] Irion FW, Kahn BH, Schreier MM, Fetzer EJ, Fishbein E, Fu D, Kalmus P, Wilson RC, Wong S, Yue Q. Single-footprint retrievals of temperature, water vapor and cloud properties from AIRS. Atmosph Meas Tech 2018;11:971–95. https://doi.org/10.5194/amt-11-971-2018.

[31] Li J, Geer AJ, Okamoto K, Otkin JA, Liu Z, Han W, Wang P. Satellite all-sky infrared radiance assimilation: recent progress and future perspectives. Adv Atmosph Sci 2022;39:9–21. https://doi.org/10.1007/s00376-021-1088-9.

[32] Maddy, E.S., King, T.S., Sun, H., Wolf, W.W., Barnet, C.D., Heidinger, A., Cheng, Z., Goldberg, M.D., Gambacorta, A., Zhang, C., Zhang, K., 2011. Using MetOp-A AVHRR clear-sky measurements to cloud-clear MetOp-A IASI column radiances. 10.1175/JTECH-D-10-05045.1.

[33] Amato U, Canditiis DD, Serio C. Effect of apodization on the retrieval of geophysical parameters from Fourier-transform spectrometers. Appl Opt 1998;37:6537–43. https://doi.org/10.1364/AO.37.006537.

[34] ATB Documents: OMI | NASA's Earth Observing System [WWW Document], n.d. URL https://eospso.nasa.gov/atbd-category/49 (accessed 2.16. 2024).

[35] Garane K, Koukouli M-E, Verhoelst T, Lerot C, Heue K-P, Fioletov V, Balis D, Bais A, Bazureau A, Dehn A, Goutail F, Granville J, Griffin D, Hubert D, Keppens A, Lambert J-C, Loyola D, McLinden C, Pazmino A, Pommereau J-P, Redondas A, Romahn F, Valks P, Van Roozendael M, Xu J, Zehner C, Zerefos C, Zimmer W. TROPOMI/S5P total ozone column data: global ground-based validation and consistency with other satellite missions. Atmosph Meas Tech 2019;12:5263–87. https://doi.org/10.5194/amt-12-5263-2019.

[36] Amato U, Masiello G, Serio C, Viggiano M. The σ-IASI code for the calculation of infrared atmospheric radiance and its derivatives. Environ Model Softw 2002;17:651–67. https://doi.org/10.1016/S1364-8152(02)00027-0.

[37] Clough SA, Shephard MW, Mlawer EJ, Delamere JS, Iacono MJ, Cady-Pereira K, Boukabara S, Brown PD. Atmospheric radiative transfer modeling: a summary of the AER codes. J Quant Spectrosc Radiat Transf 2005;91:233–44. https://doi.org/10.1016/j.jqsrt.2004.05.058.

[38] Yang P, Bi L, Baum BA, Liou K-N, Kattawar GW, Mishchenko MI, Cole B. Spectrally consistent scattering, absorption, and polarization properties of atmospheric ice crystals at wavelengths from 0.2 to 100 μm. J Atmosph Sci 2013;70:330–47. https://doi.org/10.1175/JAS-D-12-039.1.

[39] Yang P, Hioki S, Saito M, Kuo C-P, Baum BA, Liou K-N. A review of ice cloud optical property models for passive satellite remote sensing. Atmosphere (Basel) 2018;9:499. https://doi.org/10.3390/atmos9120499.

[40] Martinazzo M, Maestri T. The MAMA algorithm for fast computations of upwelling Far- and Mid-Infrared radiances in the presence of clouds. Remote Sens 2023;15:4454. https://doi.org/10.3390/rs15184454.

[41] Masiello G, Serio C, Venafra S, Liuzzi G, Poutier L, Göttsche F-M. Physical retrieval of land surface emissivity spectra from hyper-spectral infrared observations and validation with in situ measurements. Remote Sens 2018;10:976. https://doi.org/10.3390/rs10060976.
[42] Wyser K. The effective radius in ice clouds. J Clim 1998;11:1793–802. https://doi.org/10.1175/1520-0442(1998)011<1793:TERIIC>2.0.CO;2.
[43] Martin GM, Johnson DW, Spice A. The measurement and parameterization of effective radius of droplets in warm stratocumulus clouds. J Atmosph Sci 1994;51:1823–42. https://doi.org/10.1175/1520-0469(1994)051<1823:TMAPOE>2.0.CO;2.
[44] Amato U, Carfora MF, Cuomo V, Serio C. Objective algorithms for the aerosol problem. Appl Opt 1995;34:5442–52. https://doi.org/10.1364/AO.34.005442.
[45] Grieco G, Masiello G, Matricardi M, Serio C, Summa D, Cuomo V. Demonstration and validation of the φ-IASI inversion scheme with NAST-I data. Q J R Meteorol Soc 2007;133:217–32. https://doi.org/10.1002/qj.162.
[46] Borbas EE, Hulley G, Feltz M, Knuteson R, Hook S. The combined ASTER MODIS emissivity over land (CAMEL) part 1: methodology and high spectral resolution application. Remote Sens 2018;10:643. https://doi.org/10.3390/rs10040643.
[47] Masiello G, Serio C, Venafra S, DeFeis I, Borbas EE. Diurnal variation in Sahara desert sand emissivity during the dry season from IASI observations. J Geophys Res Atmosph 2014;119:1626–38. https://doi.org/10.1002/jgrd.50863.
[48] Baldridge AM, Hook SJ, Grove CI, Rivera G. The ASTER spectral library version 2.0. Remote Sens Environ 2009;113:711–5. https://doi.org/10.1016/j.rse.2008.11.007.
[49] Masuda K, Takashima T, Takayama Y. Emissivity of pure and sea waters for the model sea surface in the infrared window regions. Remote Sens Environ 1988;24:313–29. https://doi.org/10.1016/0034-4257(88)90032-6.
[50] Reuter M, Buchwitz M, Schneising O, Hase F, Heymann J, Guerlet S, Cogan AJ, Bovensmann H, Burrows JP. A simple empirical model estimating atmospheric CO_2 background concentrations. Atmosph Meas Tech 2012;5:1349–57. https://doi.org/10.5194/amt-5-1349-2012.
[51] Engel A, Bönisch H, Ullrich M, Sitals R, Membrive O, Danis F, Crevoisier C. Mean age of stratospheric air derived from AirCore observations. Atmosph Chem Phys 2017;17:6825–38. https://doi.org/10.5194/acp-17-6825-2017.
[52] Anderson, G., Clough, S., Kneizys, F., Chetwynd, J., Shettle, E., 1986. AFGL atmospheric constituent profiles (0.120km) 46.
[53] Aumann HH, Chen X, Fishbein E, Geer A, Havemann S, Huang X, Liu X, Liuzzi G, DeSouza-Machado S, Manning EM, Masiello G, Matricardi M, Moradi I, Natraj V, Serio C, Strow L, Vidot J, Chris Wilson R, Wu W, Yang Q, Yung YL. Evaluation of radiative transfer models with clouds. J Geophys Res Atmosph 2018;123:6142–57. https://doi.org/10.1029/2017JD028063.
[54] Cimini D, Serio C, Masiello G, Mastro P, Ricciardelli E, Paola FD, Larosa S, Gallucci D, Hultberg T, August T, Romano F. Spectrum synergy for investigating cloud microphysics. Bull Am Meteorol Soc 2023;104:E606–22. https://doi.org/10.1175/BAMS-D-22-0008.1.
[55] Lubrano AM, Masiello G, Matricardi M, Serio C, Cuomo V. Retrieving N2O from nadir-viewing infrared spectrometers. Tellus B 2004;56:249–61. https://doi.org/10.1111/j.1600-0889.2004.00100.x.
[56] Camy-Peyret C, Liuzzi G, Masiello G, Serio C, Venafra S, Montzka SA. Assessment of IASI capability for retrieving carbonyl sulphide (OCS). J Quant Spectrosc Radiat Transf 2017;201:197–208. https://doi.org/10.1016/j.jqsrt.2017.07.006.
[57] Serio Carmine, Masiello G, Venafra S. CO2 retrieval algorithm for the infrared atmospheric sounder interferometer: the potential of retrieving the vertical profile of carbon dioxide from its hot or laser bands in the 800-1200 cm-1 atmospheric window. In: Proceedings of the remote sensing of clouds and the atmosphere XXIV. SPIE; 2019. p. 113–25. https://doi.org/10.1117/12.2532729. Presented at the remote sensing of clouds and the atmosphere XXIV.
[58] Camy-Peyret C, Liuzzi G, Masiello G, Serio C, Venafra S, Montzka SA. Assessment of IASI capability for retrieving carbonyl sulphide (OCS). J Quant Spectrosc Radiat Transf 2017;201:197–208. https://doi.org/10.1016/j.jqsrt.2017.07.006.
[59] Serio C, Masiello G, Liuzzi G. Demonstration of random projections applied to the retrieval problem of geophysical parameters from hyper-spectral infrared observations. Appl Opt 2016;55:6576–87. https://doi.org/10.1364/AO.55.006576.
[60] Serio C, Masiello G, Mastro P, Tobin DC. Characterization of the observational covariance matrix of hyper-spectral infrared satellite sensors directly from measured earth views. Sensors 2020;20:1492. https://doi.org/10.3390/s20051492.
[61] Bormann N, Collard A, Bauer P. Estimates of spatial and interchannel observation-error characteristics for current sounder radiances for numerical weather prediction. II: application to AIRS and IASI data. Q J R Meteorol Soc 2010;136:1051–63. https://doi.org/10.1002/qj.615.
[62] Masiello G, Serio C, Antonelli P. Inversion for atmospheric thermodynamical parameters of IASI data in the principal components space. Q J R Meteorol Soc 2012;138:103–17. https://doi.org/10.1002/qj.909.
[63] Lecours M, Bernath P, Boone C, Crouse J. Infrared transmittance spectra of polar stratospheric clouds. J Quant Spectrosc Radiat Transf 2023;294:108406. https://doi.org/10.1016/j.jqsrt.2022.108406.
[64] Ackerman SA, Smith WL, Revercomb HE, Spinhirne JD. The 27–28 October 1986 FIRE IFO cirrus case study: spectral properties of cirrus clouds in the 8–12 μm window. Mon Weather Rev 1990;118:2377–88. https://doi.org/10.1175/1520-0493(1990)118<2377:TOFICC>2.0.CO;2.
[65] Smith RG, Wright CM. The librational band of water ice in AFGL 961: revisited. Mon Not R Astron Soc 2011;414:3764–8. https://doi.org/10.1111/j.1365-2966.2011.18721.x.
[66] Krämer M, Rolf C, Spelten N, Afchine A, Fahey D, Jensen E, Khaykin S, Kuhn T, Lawson P, Lykov A, Pan LL, Riese M, Rollins A, Stroh F, Thornberry T, Wolf V, Woods S, Spichtinger P, Quaas J, Sourdeval O. A microphysics guide to cirrus – Part 2: climatologies of clouds and humidity from observations. Atmosph Chem Phys 2020;20:12569–608. https://doi.org/10.5194/acp-20-12569-2020.
[67] Evan S, Brioude J, Rosenlof KH, Gao R-S, Portmann RW, Zhu Y, Volkamer R, Lee CF, Metzger J-M, Lamy K, Walter P, Alvarez SL, Flynn JH, Asher E, Todt M, Davis SM, Thornberry T, Vömel H, Wienhold FG, Stauffer RM, Millán L, Santee ML, Froidevaux L, Read WG. Rapid ozone depletion after humidification of the stratosphere by the Hunga Tonga Eruption. Science 2023;382:eadg2551. https://doi.org/10.1126/science.adg2551.
[68] Masiello G, Matricardi M, Serio C. The use of IASI data to identify systematic errors in the ECMWF forecasts of temperature in the upper stratosphere. Atmosph Chem Phys 2011;11:1009–21. https://doi.org/10.5194/acp-11-1009-2011.